AALBORG UNIVERSITET

Preview-based Asymmetric Load Reduction of Wind Turbines

Mathias B. Madsen Jakob Filsø

Intelligent Autonomous Systems
Master's thesis

May 2012

Department of Electronic Systems
Aalborg University

AALBORG UNIVERSITET

Department of Electronic Systems

Fredrik Bajers Vej 7, 9220 Aalborg Øst

Telephone +45 99 40 86 00

Title: Preview-based Asymmetric Load Reduction of Wind Turbines

Project period: September 2nd, 2011 to May 31st, 2012

Project Group:
1037

Group members:
Jakob Filsø
Mathias Bækdal Madsen

Supervisors:
Mohsen Soltani
Rafael Wisniewski

Copies: 5
Pages: 77
Attachments: 1 DVD

Synopsis

Fatigue loads on wind turbines caused by an asymmetric wind field become an increasing concern when the scale of wind turbines increases. This thesis presents a preview-based approach to reduce asymmetric loads by using Light Detection And Ranging (LIDAR) measurements. A Model Predictive Controller (MPC) is developed that utilize a preview history of the wind obtained from the LIDAR. The controller is based on a model with individual pitching of the blades, such that the asymmetric loads can be reduced by cyclic blade pitching. Using a transformation of moments acting on the blades, the controller is able to determine the pitching of the blades. This is done while still maintaining a given power reference and satisfying a set of actuator constraints. The designed controller was tested on a 5 MW wind turbine in the FAST simulation software and compared to the same controller without LIDAR data and a baseline controller for the turbine. The results showed that MPC without LIDAR performed similarly to the baseline controller and that MPC with LIDAR was able to reduce the asymmetric loads while still maintaining the power reference.

Preface

This master's thesis is written by group 1037 on the Intelligent Autonomous Systems master's program at the Department of Electronic Systems at Aalborg University.

The project has been run during the period from the 2nd of September, 2011, to the 31st of May, 2012. During the 3 month period from January to March the group has been studying abroad at Stanford University, California, USA. In this time, the group studied Convex Optimization while still working on the project.

The thesis is accompanied by a conference paper submitted to the 2012 IEEE Multi-Conference on Systems and Control. The paper has been accepted for presentation at the conference which takes place in Croatia, October 3-5, 2012.

The group would like to thank Asoc. Prof. Mohsen Soltani and Prof. Rafael Wisniewski for their supervision and guidance of the project.

Furthermore, the group would like to thank Prof. Stephen Boyd for his hospitality during our visit at Stanford University and Kathryn Johnson from NREL for providing the necessary simulation software for this project.

Mathias Bækdal Madsen

Jakob Filsø

Reading guidelines

Citations are given by the Harvard Method, e.g. (Bossanyi, 2005). The thesis is accompanied by a paper and a DVD. The DVD contains the thesis and the paper in digital form. The simulation software of the designed controller can not be provided as it has not been publicly released by NREL. A nomenclature is found in appendix A on page 69 with acronyms, abbreviations, and symbols. Headings, equations, tables, and images are numbered in the form $a.b$ where a is the chapter and b is a sequential number.

Contents

Chapter 1

Introduction

A wind turbine is a dynamic mechanical system that converts kinetic energy from the wind into electrical power. The wind causes a rotor on the wind turbine to rotate in order to produce power through a generator. An example of a modern wind turbine is the Vestas V112-3.0 MW shown in figure 1.1 (Vestas, 2012).

Figure 1.1: Vestas V112-3.0 MW wind turbine.

The wind turbine industry has been growing rapidly over the last decade as a cause of more interest in renewable energy sources (BTM Consult, 2010). With this growth, development and research in wind turbines has also risen. Wind turbine manufacturers are developing larger wind turbines with larger blade spans to reduce the cost of energy (Bianchi, De Battista and Mantz, 2007). Larger blade spans causes a reduction of the cost of energy because the power extraction from the wind grows with the square of the radius of the turbine rotor. To keep the production costs down, it is desirable for wind turbine manufacturers to use light and low cost materials. With the added size of the turbine, the structure becomes more flexible as a consequence. A problem with a larger swept rotor area is the occurance of a more asymmetric wind field in the swept rotor area, with high turbulence areas affecting only part of the swept rotor area. Local turbulence can stem from the wind itself or in the case of a wind farm from the wake of other wind turbines. This effect can be seen in figure 1.2 (Aeolus, 2008). Such asymmetry causes vibration modes of the wind turbine to be excited causing fatigue in the structure of the turbine. As it is also desired to maintain the reliability of the turbines as they grow larger, more advanced control strategies to mitigate the increased loads on the structure are necessary.

Figure 1.2: Offshore wind farm at Horns Rev with turbulence patterns visible due to unique weather conditions.

Wind turbines are designed to operate within a certain range of wind speeds. A wind speed termed the cut-in wind speed denotes the lowest wind speed at which the wind turbine operates. The power output is too low under this speed to generate a profit. Similarly, the cut-out wind speed denotes the highest wind speed at which the wind turbine operates. The cut-out wind speed exists to prevent overloading of the wind turbine. The power output is split into three regions between these two speeds. These are seen in figure 1.3 on the next page.

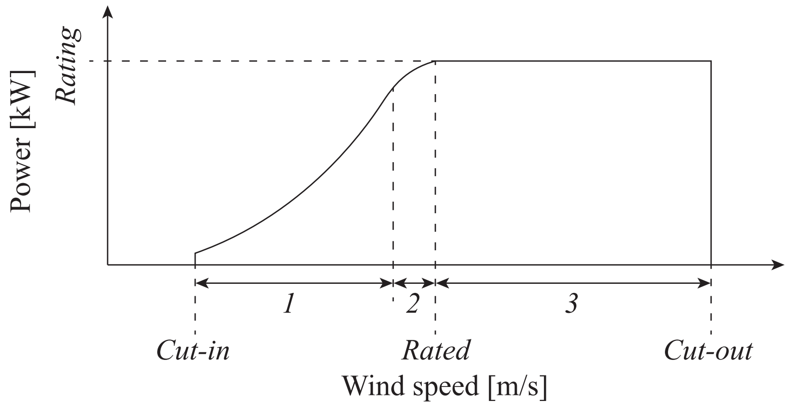

Figure 1.3: Power curve for a wind turbine.

In region 1 the energy in the wind is low and the controller is designed to maximize the power extraction from the wind. Above a certain wind speed denoted the rated wind speed, the controller limits the power production to a certain value denoted the power rating of the turbine. This limit is imposed on region 3. The reason for the limit is that the cost of energy would rise if power extraction was maximized for higher wind speed (Bianchi et al., 2007). This is because the structure would have to be more rigid and because high wind speeds occur less frequently. Region 2 acts as a transition region where the rotor speed is limited to prevent acoustic noise and to keep the centrifugal forces at a value tolerated by the blades (Bianchi et al., 2007).

Traditionally, in full load operation (region 3), the collective pitch angle of the rotor blades is adjusted to control the aerodynamic rotational torque of the rotor to keep the power generation at the power rating (Bossanyi, 2003*b*). The reference input for the collective pitch angle is controlled by a PID controller, acting on the generator speed (Johnson, Pao, Balas and Fingersh, 2006). In this case, the collective pitch control is not able to reduce asymmetric loads on the turbine. These loads appear as harmonics with frequency peaks at integer coefficients of the rotor angular velocity, $n \cdot P$. For a 3-bladed turbine, which is used in this project, the asymmetric loads appear at the $1P$ frequency as well as higher order harmonics. For large scale wind turbines, the loads at the $1P$ frequency contribute very significantly to the fatigue loads on the structural components of the wind turbine, and is therefore of great interest (Bossanyi, 2003*a*). The works in (Bossanyi, 2005), (Kanev and van Engelen, 2010), and (Jelavić, Petrović and Perić, 2010) show that the $1P$ frequency loads can be reduced by adding a correction to the reference command of individual pitch references.

1.1 Project Focus

This project shows how $1P$ asymmetric loads can be reduced by utilizing a Light Detection and Ranging (LIDAR) module. A LIDAR provides wind measurements in front of the turbine, such that preview measurements of the wind disturbances are obtained. Model Predictive Control will be used as a framework for the preview information, as this control method is able to predict the wind turbines behavior based on the preview measurements. To make it possible to reduce the asymmetric loads, individual pitch references to the blades will be used. The project will be constrained by considering only region 3 where the wind disturbances are largest, although it may be possible to extend the control scheme to region 1 and 2.

The results of the proposed controller are compared to MPC without the LIDAR information and compared to a traditional baseline controller with collective pitching. The high fidelity aeroelastic wind turbine simulation software FAST (Jonkman and Jr., 2005) from the National Renewable Energy Laboratory (NREL) is used with a fictive 3-bladed reference turbine with a power rating of 5 MW (Jonkman, Butterfield, Musial and Scott, 2009).

1.2 Related Work

In (Soltani, Wisniewski, Brath and Boyd, 2011), (Laks, Pao, Simley, Wright, Kelley and Jonkman, 2011), and (Dunne, Simley and Pao, 2011) the LIDAR showed potential for the reduction of loads on the wind turbine structure. However, these consider only collective pitching of the blades. Individual pitching have been used in (Bossanyi, 2005), (Kanev and van Engelen, 2010), and (Jelavić et al., 2010) to obtain reductions of the $1P$ harmonic loads. This project proposes the use of LIDAR to reduce asymmetric loads by providing preview information used for individual pitching through MPC.

1.3 Outline of the Thesis

The thesis is organized as follows: Chapter 2 gives an overview of the components of a wind turbine, wind fields, aerodynamic loads, and the FAST simulation software. In chapter 3 the LIDAR module is presented. The different types of LIDARs and configurations are presented along with some important limitation of LIDARs. The LIDAR configuration used for the controller will also be presented. The model used for MPC is described in chapter 4. This involves modeling of the aerodynamics of the individual blades along with modeling of the components and structure. Chapter 5 presents the proposed controller and shows a simple method to include the asymmetric loads in MPC. The results of the controller is presented in chapter 6 together with a discussion of the results. Finally, the project is concluded in chapter 7.

Chapter 2

Overview of Wind Turbines

This chapter will provide an overview of important and fundamental aspects of wind turbines. Basic terminology will be introduced and the components of a wind turbine will be presented. As asymmetries in the wind field is of interest in this project, some of the causes of these will be presented. The aerodynamic loads on the wind turbine will be presented as well. Finally, a short introduction to the wind turbine simulation software used for this project will be given.

2.1 Configurations and Components

Broadly speaking, there are two types of wind turbines: Vertical-axis wind turbines (VAWTs) and horizontal-axis wind turbines (HAWTs). Of these HAWTs are most commonly used (Bianchi et al., 2007) and are also used in this project. The basic terminology of these will be presented briefly. Figure 2.1 on the following page shows the basic structural components of a HAWT.

For a HAWT, the wind turbine rotor is placed on a tower. The rotor is usually placed upwind of the tower to avoid the turbulence the tower generates. The blades are mounted on the hub which rotates with the blades. HAWTs most commonly have 3 blades. The term variable pitch is used if it is possible to pitch the blades, and conversely, fixed pitch is used if it is not possible. Collective pitch is used to denote that the blades can only be pitched at the same angle, with individual pitch denoting that an individual pitch angle reference can be given to each blade. The rotor (that is, hub and blades) is connected to the nacelle through a shaft which drives the generator. The generator resides within the nacelle along with several other components. In figure 2.2 on the next page, some of the typical components of the nacelle are shown.

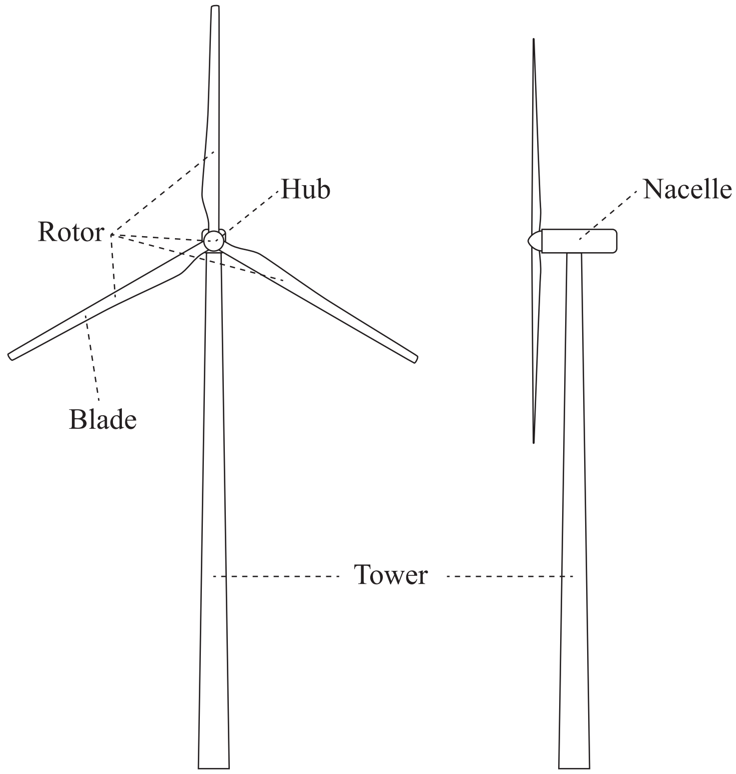

Figure 2.1: Horizontal-axis wind turbine and its basic components.

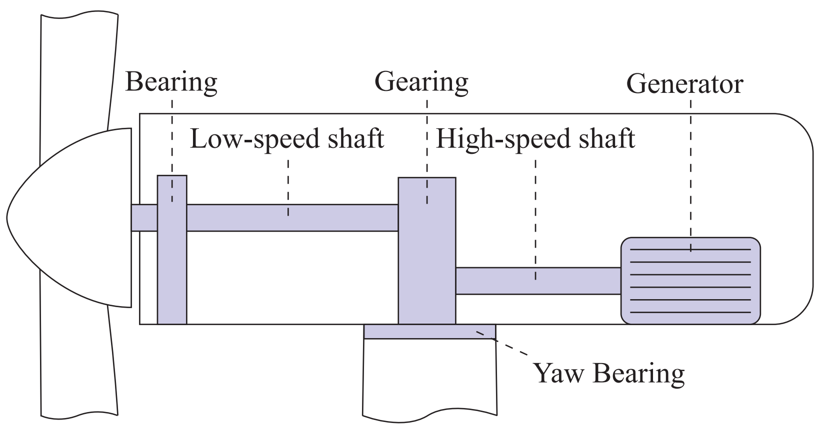

Figure 2.2: Selected nacelle components.

The rotor is connected to the low-speed shaft. A bearing is placed around the low-speed shaft to support the rotor. As the generator operates at higher rotational speeds than the rotor, a high-speed shaft is connected to it. A gearing couples the low-speed shaft and the high-speed shaft. Finally, a yaw bearing connects the tower with the nacelle and provides the possibility for yawing the turbine. It should be noted that there are several other components present in the nacelle, such as brakes, yaw motor etc. However, these are not relevant for this project and will not be presented.

The generator on modern wind turbines is usually decoupled from the power grid, so it is possible for the wind turbine to operate at other rotational speeds than the one corresponding to the grid frequency. If this is the case the wind turbine is termed variable-speed, with fixed-speed being the opposite case.

For this project a variable-speed variable-pitch 3-bladed HAWT is considered. The blades can be pitched individually and the rotor turns clockwise when looking in the downwind direction.

2.2 Wind Fields

As the swept area of the rotor grows larger, so does the variations in the wind speed in this area. Variations in the wind speed are caused by a variety of factors such as turbulence in the wind, wind shear, tower shadow, and wake effect from other turbines.

Wind speed fluctuations with a relatively high frequency are called turbulence. Turbulence has a major impact on the aerodynamic loads on the blades as different regions of the blades are excited by different wind speeds (Bianchi et al., 2007).

Wind shear is the difference in speed and direction of the wind over a relatively short area. For wind turbines wind shear is present and have more effect on larger rotor areas. The most dominant type of wind shear for wind turbines is the presence of the ground which delays the wind at lower heights, causing a higher mean wind speed at higher altitudes (Bianchi et al., 2007).

With the tower placed downwind of the rotor, the wind at the rotor is changed as it flows around the tower. This results in a decrease in the wind speed in the axial (or downwind) direction as the lateral component of the wind become larger. This effect is called tower shadow and is also a cause for asymmetry in the wind field. It should be noted that because LIDARs measure at a certain distance in front of the turbine, the tower shadow effect on the speed is not included in these measurements.

Finally, if other wind turbines are present in front of the turbine, which is the case for wind farms, a so-called wake effect can influence the turbine. When wind turbines extract energy from the wind the wind loses axial speed. This results in local areas of slower wind speeds. The rotor also affects the direction of the wind.

The rotating blades induce forces on the wind which causes wind turbulence that rotate in the opposite direction of the rotor.

2.3 Aerodynamic Loads

The wind induces different loads on the wind turbine. Even if the wind field is uniform, meaning that the speed is the same over the entire rotor disc at a particular time, the wind turbine will still experience fatigue due to the change in wind speed over time. These variations in wind speed will mainly cause bending of the blades and tower together with torsion in the low-speed shaft. As LIDARs provide a preview of this variation in wind speed, it is possible to mitigate these loads with a LIDAR.

Consider now a wind field with variations in the wind speed over the rotor disc (corresponding to the swept rotor area). If the distribution of the wind speed is such that the blades are excited by different wind speeds at a point in time, the wind speed is called asymmetric with respect to the blades. The loads induced on the wind turbine by such a wind field will be called asymmetric loads. These loads will appear as harmonics dependent on the rotational speed of the rotor. This is because the individual blades samples the whole wind field with every revolution of the blades. The term rotational sampling is used for this effect (Bianchi et al., 2007). The frequency for the revolutions of a single blade is termed the $1P$ frequency. The frequency of which all 3 blades passes a point on the rotor is termed the $3P$ frequency.

Loads at the $1P$ frequency together with harmonics of $2P$, $3P$, $4P$ etc. appear on the blades as they rotate. For a three-bladed rotor, the rest of the structure only experience the harmonics of $3P$, $6P$, $9P$ etc. as $1P$ and the other harmonics tend to cancel out because of the averaging effect of the rotor (Bossanyi, 2003*a*). However, if the turbulence is changing such that the blades don't experience the same wind speeds, the $1P$ loads will also propagate through the structure and cause fatigue for several structural components. For large scale wind turbines, the $1P$ components of the loads can cause significant fatigue (Bossanyi, 2003*a*), and is why it is the main interest for this project.

2.4 FAST Design Codes

The wind turbine simulator used in this project is the Fatigue, Aerodynamics, Structures, and Turbulence (FAST) simulator. It is an aerolastic simulator capable of simulating a variety of different wind turbines. FAST is capable of showing a variety of different loads of the wind turbine along with many other performance variables. The FAST edition used in this project is a special edition kindly provided by NREL with a LIDAR module added to the standard FAST. FAST is accompanied by a stochastic wind field generator called TurbSim (Jonkman, 2009) which is used in this project to generate wind fields for test with the designed controllers.

2.4.1 NREL 5 MW wind turbine

The wind turbine used is the fictive NREL 5 MW wind torbine (Jonkman et al., 2009) which is based on several commercial wind turbines. Specifications for the 5 MW wind turbine are shown in table 2.1.

Power rating	5 MW
Blades	3 with individual pitch
Rotor diameter	126 m
Hub height	90 m
Cut-in/Cut-out speed	3 m/s , 25 m/s
Cut-in/rated rotor speed	6.9 rpm , 12.1 rpm

Table 2.1: Specifications of the NREL 5 MW wind turbine.

2.4.2 Baseline Controller

For the NREL 5 MW wind turbine NREL has designed a baseline controller. The baseline controller is a collective pitch controller designed for both below rated operation (region 1 and 2) and at rated operation (region 3). The controller is a PI controller with gain scheduling determined by the generator speed. In region 1 it is designed to set the pitch angle to zero and only use the generator torque to maximize power. In region 3 the controller uses the collective pitch angle to limit the power production to 5 MW. The only measured output used for the controller is the generator speed.

Chapter 3

LIDAR Systems

The objective of the Light Detection and Ranging (LIDAR) system is to provide a wind preview for each of the three blades for a preview based controller. A preview measurement is wanted for each of the blades at each time step. The LIDAR technology is based upon the principle of emitting a beam of light and measuring the backscatter of the particles hit by the beam, thereby determining the speed of the particles based on the Doppler effect. LIDAR systems differ in sampling rate, effective measurement distances, and the technology they use to achieve the measurements. The LIDAR can also be mounted in different positions on the wind turbine and at different elevation angles, which both have a huge impact on the performance. The LIDAR technology also have a lot of limitations and if these are not dealt with they can potentially make the LIDAR measurements faulty and cause worse performance than without LIDAR. All of these topics will be covered in this chapter.

3.1 Types

There exists two types of LIDAR technologies: Continuous Wave (CW) LIDAR and Pulsed LIDAR . Each have different drawbacks and advantages. Both

Continuous wave LIDAR

The CW LIDAR works by focusing the beam of light at a given focal distance and is only able to measure the wind at focal point. The focal distance plays a key role for the effectiveness of CW LIDAR since the CW LIDAR acts as a low-pass filter for all the wind speeds along beam centered arund the focal distance. By increasing the focal distance the error on the measurements increases as well. According to (Simley, Pao, Frehlich, Jonkman and Kelley, 2011) CW LIDAR works well for focal distances between 10 m and 200 m. Above 200 m the CW LIDAR acts as a mean wind estimator and is unable to measure fluctuations in the wind field. The CW is able sample very fast (50 Hz) since it is able to emit light and detect simultaneously (Braña, 2001).

By measuring a circle with scan radius, r at a distance D, called the preview distance, in front of the LIDAR and parallel to the rotor disc, a spiral of measurements is created due to the wind field moving towards the wind turbine and the CW LIDAR is mounted on a spinner so it rotates. The elevation angle θ_{el} of the measurements is shown in figure 3.1 along with preview distance and radius of the sampled circle.

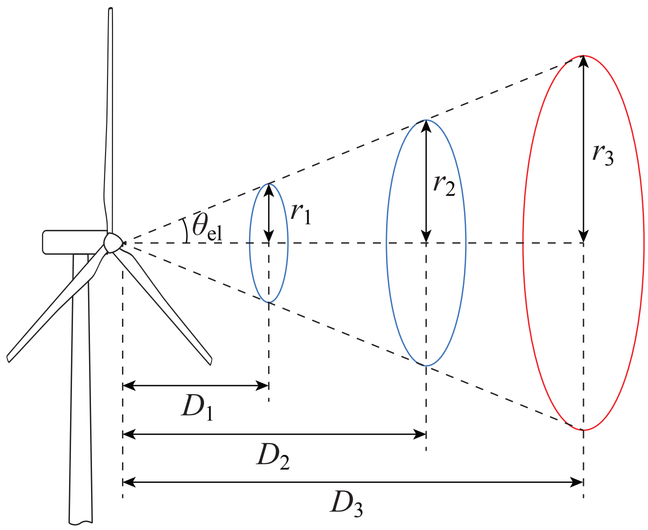

Figure 3.1: Multiple preview distances D for Pulsed LIDAR (blue) with a fixed elevation angle θ_{el} and a single preview distance for CW LIDAR (red) with the same elevation angle.

The elevation angle is determined by the radius and preview distance by the geometric relationship

$$\theta_{\text{el}} = \arctan\left(\frac{r}{D}\right), \tag{3.1}$$

as shown in figure 3.1.

Pulsed Lidar

The Pulsed LIDAR works by emitting a pulse of light at the target location. Since the speed of light is constant it is known at which time the pulse is back, this enables the Pulsed LIDAR to select a target distance or a multiple of target distances, along the beam of light. The Pulsed LIDAR is able to measure at great distances in the order of 2000 m since the measurement error does not increase with preview distance as it does with CW LIDAR (Simley et al., 2011). The ability to measure at great preview distances together with the ability to measure at multiple distances makes it great for measuring an entire wind field. Different preview distances with a fixed elevation angle θ_{el} is shown in figure 3.1 on the preceding page.

The elevation angle is determined by (3.1) just as for CW LIDAR. The sampling rate of the Pulsed LIDAR is significantly slower (1 Hz) than that of the CW LIDAR. However Pulsed LIDAR is able measure multiple points at the same time.

3.2 Mounting on the Wind Turbine

The LIDAR module can be mounted several different places on the wind turbine. If mounted on top of the nacelle it is not possible to measure all the time due to blades blocking the signal. When mounted on the hub the rotor no longer blocks the LIDAR. Both the nacelle and the hub mounted LIDAR are normally placed on a spinner to create circles at which they sample. The nacelle mounted LIDAR and the hub mounted both suffer from the Cyclops dilemma, where the LIDAR is only able to measure the line of sight (LOS) velocity of the wind. This can be circumvented by using multiple LIDARs and mounted with a significant distance between them. This can be done by mounting the LIDARs in the blades. The drawback by mounting the LIDARs in the blades is the increased complexity and higher cost of implementation. Usually only one LIDAR is used which measures LOS. The measurements are then projected onto the axial direction (perpedicular to the rotor plane).

3.3 Limitations

The LIDAR has several limitations that can severely influence the measurements and thus influence the performance of the controller. Some of those limitations can make the measurements so faulty that they actually worsen the performance of the controller compared to controllers without LIDAR. Some of the major limitations of LIDAR and sources of error are listed here.

Alignment of the wind turbine

When the wind turbine is not facing upwind the LIDAR measures a wind field that will not be propagated to the wind turbine, thus the measurements do not contain any information of the wind field that will affect the wind turbine. This causes the controller to act on wrong information.

Vertical and lateral wind components

If the vertical and lateral components of the wind field are large compared to the axial wind speed errors are introduced because the LIDAR measures LOS and projects the measurements into the axial direction.

Elevation angle

As the LIDAR only measures line of sight a large elevation angle will make the LIDAR very sensitive to vertical and lateral components of the wind (Simley et al., 2011).

Propagation time

If the measurements do not propagate with the mean speed the measured data do not represent the winds affecting the wind turbine at the correct time. If the preview distance is large the possiblility of the wind changing characteristics, from the time the data are measured to the time time the wind hit the wind turbine, will increase, thus introducing unceartainty in the measurements.

Working conditions

The LIDAR have difficulties measuring in clear weather conditions since there are fewer particles in the atmosphere for the light to backscatter from. The CW LIDAR has problems with backscatter from low clouds as well (Braña, 2001).

3.4 Choice of Configuration

The configuration for this project is chosen to be a CW LIDAR setup with preview distance of 54 m and an elevation angle of 41.2 °, as the circle sampled has a radius of $0.75R$ (47.25 m). When considering preview distance of the CW LIDAR it is important to choose the correct r. The scan radius should be chosen so it represents the fraction of the blade that has the most influence. The scan radius should be chosen to be about 75 % of the rotor radius R according to (Laks, Pao, Wright, Kelley and B.Jonkman, 2010), because the maximum power extraction is at around 75 %. The elevation angle must not be too large since that can introduce measurement errors according to (Simley et al., 2011) and should be smaller and than 45°.

CW LIDAR is chosen because it has a low measurement error compared to the Pulsed LIDAR at short distances and is able sample very fast at a given preview distance, which makes it suitable for the controller of this project. The reason 54 m

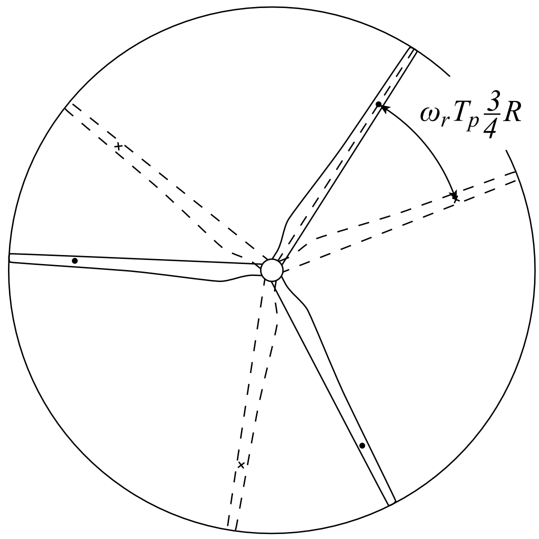

Figure 3.2: LIDAR measurement positions (crosses) in the rotor plane. Measurements are taken $\omega_r T_p$ radians ahead of the blades and at 75 % blade span.

is chosen as preview distance is that the wind data used in this project has a mean wind speed of 18 m/s which gives a preview horizon of 3 seconds. The 3 seconds are chosen so the elevation angle is not too large.

When obtaining a time history of the wind speeds, the predicted positions of the blades need to be taken into account. Because of this, the position of the measurements in the rotor plane is $\omega_r T_p$ radians ahead of each blade. This is shown in figure 3.2.

As mentioned earlier the LIDAR technology has a lot of limitations. In order to use LIDAR for the controller some assumptions are needed:

- The mean wind direction is perfectly aligned with the wind turbine, meaning that the lateral and vertical wind speeds both have zero mean in the preview horizon.

- Turbulence moves with the mean wind speed and direction and the turbulence does not grow or fade in the preview horizon (Taylor's Frozen Turbulence Hypothesis). This assumption is both used in the design of the controller and in the simulation.

- It is assumed that the vertical and lateral components of the wind field are negligible compared to the axial.

- It is assumed that the weather conditions are sufficient for LIDAR to be used.

Figure 3.3 shows preview wind measurements of the CW LIDAR compared to the actual wind speed of a blade at 75 % span. The figure shows that CW LIDAR is able provide good quality preview information with the chosen preview distance and elevation angle. The data from figure 3.3 is from the FAST CW LIDAR module.

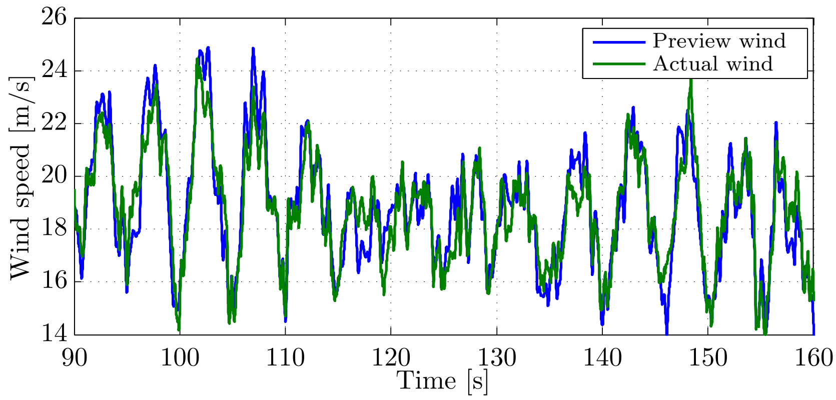

Figure 3.3: Comparison of preview wind speeds and actual wind speeds for a blade at 75 % blade span.

Chapter 4

Modeling of the Wind Turbine

The model of the wind turbine, used for the design of the controller, is outlined in this chapter. The model will be derived from mechanical, electrical, and aerodynamic models as well as a transformation to make the model suitable for the controller. To ensure that the important characteristics of the wind turbine are captured, the model will be verified against the FAST model of the 5 MW turbine presented in section 2.4 on page 10.

Since the 5 MW FAST model is used as a test bench for the developed controller, the model derived in this chapter will be developed for a configuration corresponding to the 5 MW turbine. That is, a horizontal-axis variable-speed variable-pitch turbine is considered. Yaw dynamics are not included in the model and are not considered for this project.

The model can be viewed as subsystems with signals connecting the systems. A block diagram of this abstraction with inputs, disturbances, and the most relevant outputs is shown in figure 4.1.

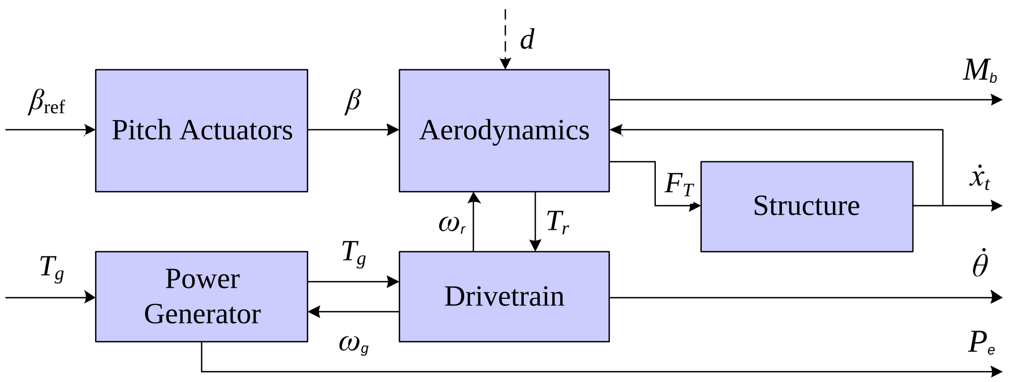

Figure 4.1: Block diagram of the model.

The aerodynamics are excited by a wind disturbance vector $d = (V_1, V_2, V_3)^T$, with the component V_1 referring to the wind disturbance on the first blade. The blade pitch vector $\beta = (\beta_1, \beta_2, \beta_3)^T$ and the axial blade moment vector $M_b = (M_{b1}, M_{b2}, M_{b3})^T$ are referenced to the blades in the same way. The axial blade moments are used to reduce the asymmetric loads as will later be described.

Translational dynamics for the fore-aft tower deflection is described in the structure system, which takes the thrust force F_T as input and produce the horizontal tower velocity $\dot{x}_t$. This velocity is fed back to the aerodynamics subsystem to generate the relative horizontal wind speed caused by the tower movement.

Closed-loop dynamics control the blade pitch vector β according to the blade pitch reference vector β_{ref}. Together with constraints on β and $\dot{\beta}$ these constitute the pitch actuators subsystem.

The rotational torque of the rotor T_r is input to the drivetrain, which together with the generator torque T_g determines the rotational speed of the rotor ω_r and the generator ω_g. A simple relationship between these rotational speeds describes the low-speed shaft torsion θ of which the time derivative $\dot{\theta}$ is of interest as it is an unwanted load on the turbine.

The power generator subsystem describe the power output P_e of the wind turbine as a function of the controllable generator torque T_g and the generator rotational speed ω_g.

The individual subsystems will be treated in the following sections. Finally, paramaters for the model is presented along with a verification of the model.

4.1 Aerodynamics

The aerodynamics of a wind turbine capture the wind energy and converts it into rotational energy through the blades. The rotor blades of the wind turbine are excited by the wind field which gives rise to forces and moments upon the structure and mechanical components of the turbine. The rotational torque T_r is the desired component of the aerodynamics. Other undesired components include bending of the tower, torsion in the drivetrain and different types of deflections of the rotor blades.

The chosen LIDAR configuration from chapter 3 on page 13 provides three wind inputs, one for each blade. The aerodynamics must therefore be described for a single blade, such that each blade contribute seperate forces and moments. Modeling the aerodynamics of the blades can be done by using the Blade Element Momentum (BEM) method which is an extension of the momentum theory for an ideal rotor. First, the momentum theory will be presented, whereafter the BEM method will be introduced to derive a model useful for the LIDAR input. These sections are based on theory from (Bianchi et al., 2007) and (Hansen, 2008).

4.1.1 Momentum Theory

Before deriving the aerodynamic model using the BEM method, it is useful to describe the aerodynamics of an ideal rotor first. By an ideal rotor is meant that the rotor simply extracts energy from the wind without causing rotation in the wake. The rotor is modeled as a disc, which is immersed in an airflow assumed to be incompressible. The mass flow rate is assumed to be the same along the airflow. The disc extracts some of the kinetic energy of the airflow resulting in a speed drop of the airflow. The airflow through the disc is shown in figure 4.2, which also shows the coresponding change in the cross-sectional area of the airflow tube. The wind speed V_0 and the area A_0 are the free stream wind speed and the airflow area in front of the rotor disc, respectively. Similarly V_D and A_D denote the wind speed and area at the disc. Lastly, $V_{-\infty}$ and $A_{-\infty}$ are the wind speed and area far behind the rotor disc.

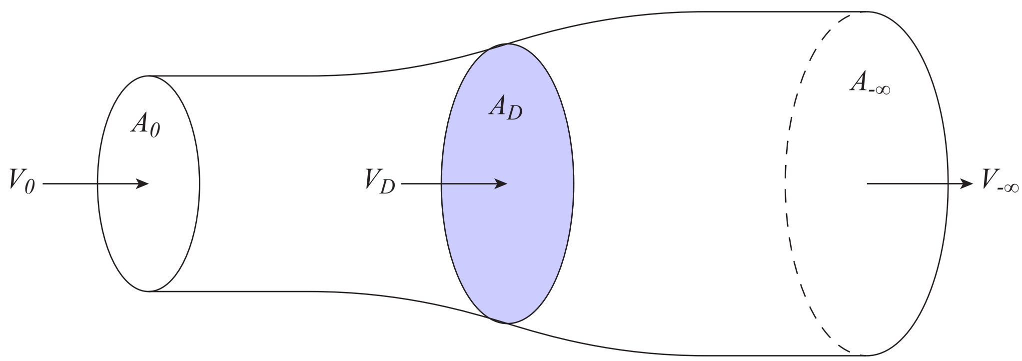

Figure 4.2: Airflow through the rotor disc.

The disc causes both changes in speed of the airflow and a change in pressure on each side of the disc as seen in figure 4.3 on the following page.

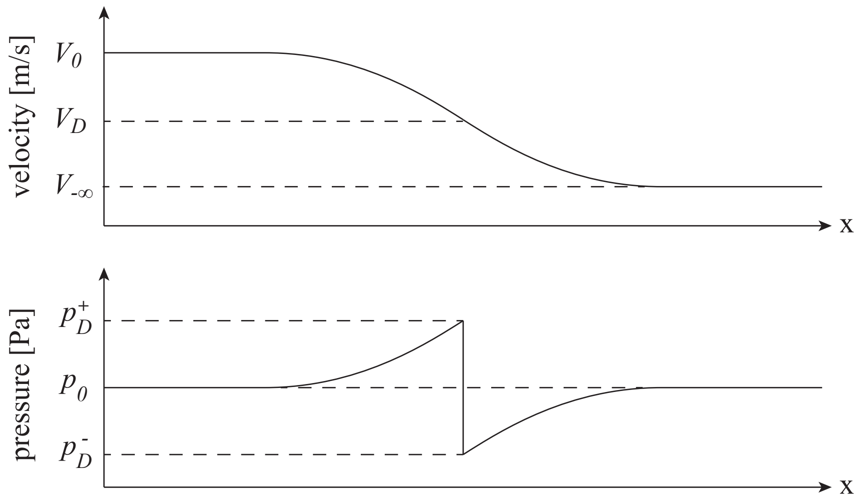

Figure 4.3: The velocity and pressure along the airflow.

The pressure drop can be expressed by Bernoulli's equation applied on each side of the disc as

$$\begin{aligned} \frac{1}{2}\rho V_0^2 + p_0 &= \frac{1}{2}\rho V_D^2 + p_D^+ \\ \frac{1}{2}\rho V_{-\infty}^2 + p_0 &= \frac{1}{2}\rho V_D^2 + p_D^-, \end{aligned} \tag{4.1}$$

where

- p_0 is the atmospheric pressure [Pa].
- p_D^+ is the pressure increase immediatly in front of the disc [Pa].
- p_D^- is the pressure decrease immediatly behind the disc [Pa].
- ρ is the density of the air [$\frac{\text{kg}}{\text{m}^3}$].

Combining the set of equations in (4.1) yields an expression for the pressure drop over the disc given by

$$\Delta p = \frac{1}{2}\rho(V_0^2 - V_{-\infty}^2). \tag{4.2}$$

With the pressure drop known it is possible to express the force developed on the disc F_D as

$$F_D = \Delta p A_D. \tag{4.3}$$

The force can also be expressed by the speed drop $(V_0 - V_{-\infty})$ as

$$F_D = (V_0 - V_{-\infty})\rho A_D V_D, \tag{4.4}$$

The wind speed at the rotor disc is usually described as

$$V_D = (1 - a)V_0, \tag{4.5}$$

where a is the axial induction factor [$\cdot$]. The axial induction factor describes how much the rotor slows down the free stream wind before reaching the rotor. By combining (4.2)-(4.5) an expression for the wind speed far behind the wind turbine is obtained as

$$V_{-\infty} = V_0(1 - 2a). \tag{4.6}$$

This shows that half of the speed drop occurs in front of the wind turbine and the other half behind the turbine. It is seen from (4.6) that momentum theory is only applicable up to $a = 0.5$. If a would be larger it would suggest that the speed far behind the wind turbine would be negative.

With the expression for $V_{-\infty}$, the force F_D from (4.4) is now expressed as

$$F_D = 2\rho A_D V_0^2 a(1 - a). \tag{4.7}$$

An expression for the power captured by the rotor disc P_D is needed to establish operating points for the model in section 4.6.2 on page 36 and is given by

$$P_D = F_D V_D = 2\rho A_D V_0^3 a(1 - a)^2. \tag{4.8}$$

The captured power is usually exressed using a power coefficient C_P. Equation (4.8) is rewritten to include C_P as

$$P_D = \frac{1}{2}\rho A_D C_P(\lambda, \beta_c) V_0^3, \tag{4.9}$$

where

- $\lambda = \omega_r R/V_0$ is tip speed ratio [$\cdot$].
- ω_r is the rotor speed [rad/s].
- R is the rotor radius [m].
- β_c is the collective pitch of the rotor blades [°].

So far only the axial induction factor of the wind turbine has been considered. When the rotor disc is not considered ideal, the rotor will induce rotation on the wind in the wake. The wind in the wake will rotate in the opposite direction of the rotor. The induced rotation speed of the wind at rotor is expressed as

$$V_{rot} = a'\omega_r r_l, \tag{4.10}$$

where

- a' is the tangential induction factor [$\cdot$].
- r_l is a local radius of the rotor disc [m].

With the induction factors and the wind speed components at the rotor disc derived, it is now possible to extend the momentum theory with the BEM method.

4.1.2 Blade Element Momentum Method

The momentum theory is now extended with the BEM method. In the BEM method the rotor disc is split into a number of annular elements N_B with seperate aerodynamic properties. Forces and moments are then found using momentum theory on each element. The BEM method uses the assumption that there are no annular aerodynamic interaction between the annular elements. The annular elements are assumed to be composed of an infinite number of blades.

The division of a blade into a finite number of elements is shown in figure 4.4, where r_j is the distance from the hub center to the center of the j'th element and Δr_j is the length of the j'th element.

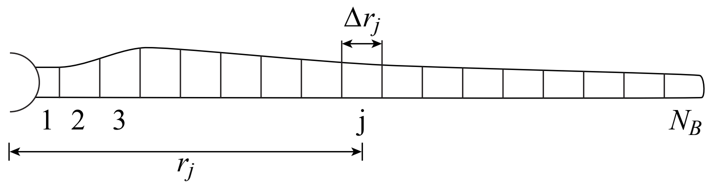

Figure 4.4: Decomposition into blade elements. The distance r_j is from the hub center to the center of the j'th element and Δr_j is the length of the j'th element.

Each blade element describe the aerodynamic properties of the corresponding annular element.

The incoming relative free stream wind speed V_w that the wind turbine experiences is dependent on the horizontal tower velocity $\dot{x}_t$ in the downwind direction (see figure 4.7), and is given by

$$V_w = V_0 - \dot{x}_t. \tag{4.11}$$

The effective wind speed that each annular element is exposed to depends on the angular velocity of the rotor ω_r, together with (4.5) and (4.10). The induction factors are now specific for each annular element and will be denoted a_j and a'_j. By looking at figure 4.5 on the facing page the effective wind speed for the annular element j is seen to be

$$V_{\text{eff,j}} = \frac{V_w(1-a_j)}{\sin(\phi_j)} = \frac{\omega_r r_j(1+a'_j)}{\cos(\phi_j)}, \tag{4.12}$$

where the local inflow angle ϕ_j is the angle between the effective wind speed and the rotor plane as shown in figure 4.5.

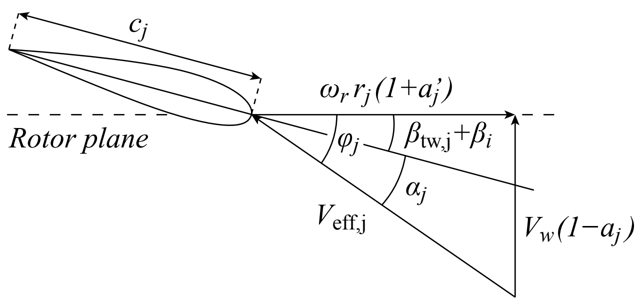

Figure 4.5: Wind components and angular quantaties for blade element j.

The local angle of attack shown in figure 4.5 is defined as $\alpha_j = \phi_j - \beta_{\text{tw,j}} - \beta_i$, where $\beta_{\text{tw,j}}$ is the local twist angle of the blade element and β_i is the pitch angle of the i'th blade . Each blade element is affected by a lift and a drag force. The drag force points in the direction of the effective wind speed and the lift force is perpendicular to it. The lift and drag forces on a blade element, L_j and D_j, are found using coefficient curves $C_{l,j}(\alpha_j)$ and $C_{d,j}(\alpha_j)$ and are given by

$$\begin{aligned} L_j &= \frac{\rho}{2} V_{\text{eff,j}}^2 c_j C_{l,j}(\alpha_j) \\ D_j &= \frac{\rho}{2} V_{\text{eff,j}}^2 c_j C_{d,j}(\alpha_j), \end{aligned} \tag{4.13}$$

where c_j is the chord length of the j'th element shown in figure 4.5.

The rotational torque $T_{\text{r,i}}$, thrust force $F_{\text{T,i}}$, and axial bending moment $M_{\text{b,i}}$ for the i'th blade are now found by summation of the contributions from each blade element. $T_{\text{r,i}}$ is used for the drivetrain model as input to the low-speed shaft. $F_{\text{T,i}}$ is the input to the fore-aft tower deflection model. Finally, $M_{\text{b,i}}$ is the blade moment used for describing the asymmetric loads. This will described in more detail in section 4.2.1 on page 28. $T_{\text{r,i}}$, $F_{\text{T,i}}$, and $M_{\text{b,i}}$ are expressed as

$$T_{\mathrm{r,i}} = \sum_{j=1}^{N_B} \left(L_j \sin(\phi_j) - D_j \cos(\phi_j)\right) r_j \Delta r_j \tag{4.14}$$

$$F_{\mathrm{T,i}} = \sum_{j=1}^{N_B} \left(L_j \cos(\phi_j) + D_j \sin(\phi_j)\right) \Delta r_j \tag{4.15}$$

$$M_{\mathrm{b,i}} = \sum_{j=1}^{N_B} \left(L_j \cos(\phi_j) + D_j \sin(\phi_j)\right) r_j \Delta r_j. \tag{4.16}$$

To calculate (4.14), (4.15), and (4.16) for a given wind speed, rotational speed, and blade pitch angle, the local inflow angle, axial induction factor, and tangential induction factor are needed for each element. By rewriting (4.12) the local inflow angle is obtained by

$$\phi_j = \arctan\left(\frac{(1-a_j)V_w}{(1+a'_j)\omega_r r_j}\right). \tag{4.17}$$

Thus, the local inflow angle is dependent on the induction factors. With the BEM method these are expressed as

$$a_j = \left(\frac{4F_P \sin(\phi_j)^2}{\sigma_j C_n} + 1\right)^{-1} \tag{4.18}$$

$$a'_j = \left(\frac{4F_P \sin(\phi_j)\cos(\phi_j)}{\sigma_j C_t} - 1\right)^{-1}, \tag{4.19}$$

where

- F_P is the Prandtl approximation for tip and root loss factors [·].
- σ_j is the solidity [·].
- C_n is the axial force coefficient [·].
- C_t is the tangential force coefficient [·].

Introducing the Prandtl approximation in the expression for the induction factors removes the assumption of an infinite number of blades. The Prandtl approximation consists of tip and root losses (F_{tip} and F_{root}) and is given by

$$F_{\mathrm{tip}} = \frac{2}{\pi}\arccos\left(e^{-\frac{B}{2}\frac{R-r_j}{r_j \sin(\phi_j)}}\right) \tag{4.20}$$

$$F_{\mathrm{root}} = \frac{2}{\pi}\arccos\left(e^{-\frac{B}{2}\frac{r_j-1}{r_j \sin(\phi_j)}}\right) \tag{4.21}$$

$$F_P = F_{\mathrm{tip}} F_r F_{\mathrm{root}}, \tag{4.22}$$

where B is the number of blades.

The solidity is the fraction of the annular area that the blades at the local radius are sweeping and is given by

$$\sigma_j = \frac{c_j B}{2\pi r_j}. \tag{4.23}$$

The axial and tangential force coefficients, C_n and C_t, are given by

$$C_n = C_l(\alpha)\cos(\phi_j) + C_d(\alpha)\sin(\phi_j) \tag{4.24}$$

$$C_t = C_l(\alpha)\sin(\phi_j) - C_d(\alpha)\cos(\phi_j). \tag{4.25}$$

4.1.3 Algorithm for computing induction factors

As seen, the induction factors are dependent on the local inflow angle and vice versa. This makes it very difficult to make a closed-form expression for the aerodynamics of the wind turbine. Instead the equations are solved iteratively by following these steps:

1. Choose ω_r, V_w, and β_i
2. Initialize a and a' to 0 (a and a' are vectors of size N_B).
3. Calculate ϕ by (4.17) (ϕ is a vector of size N_B).
4. Calculate a and a' by (4.18) and (4.19).
5. Exit if the changes in a and a' are less than a given tolerance. Otherwise, go to step 3.

4.2 Structure

The structure of a wind turbine is a flexible system with several degrees of freedom (DOF) of the blades, the tower and the drivetrain. If it is desired to reduce the structural loads of these, it is necessary to somehow include these into the model of the system.

For large scale wind turbines the asymmetric loads become increasingly interesting to mitigate. One approach to reduce these loads is to model each individual load that stems from the asymmetric loading from the wind field. This can quickly become cumbersome, and a different approach has therefore been chosen for this project. Instead, the axial blade moments $M_{\mathrm{b,i}}$ from (4.16) are transformed via the Coleman transformation to produce axial blade moments in a nonrotating reference frame. This transform will be described in 4.2.1 on the following page.

An important stress that isn't caused by the asymmetric loads is the deflection of the tower in the downwind direction caused by the thrust force on the blades. The model for the deflection is presented in section 4.2.2 on page 30.

4.2.1 The Coleman Transformation

The Coleman Transformation, or the Multi-Blade Coordinate Transformation as it is also called, is a way to transform quantities from a rotating reference frame to a nonrotating reference frame (Bir, 2008). That is, it is possible to transform the behavior from the individual blades to quantities describing the cumulative behavior of the rotor. This is desirable as will become clear shortly.

First, consider the azimuth angle of the i'th blade. For a B-bladed rotor this angle can be written as

$$\psi_i = \psi_1 + \frac{2\pi}{B}(i-1) \tag{4.26}$$

where

- ψ_i is the azimuth angle of the i'th blade [rad].
- ψ_1 is the azimuth angle of the first blade (If $\psi_1 = 0$ the blade is vertical up. See also figure 4.6.) [rad].

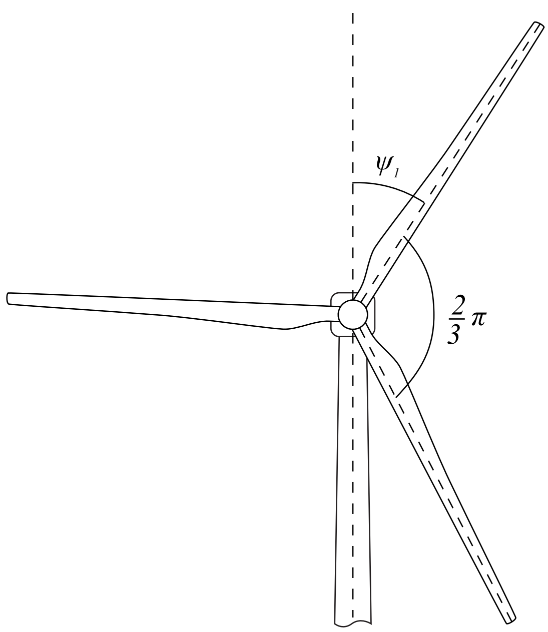

Figure 4.6: Azimuth angle of the first blade.

For a three-bladed rotor the azimuth angles of the second and the third blade become

$$\psi_2 = \psi_1 + \frac{2\pi}{3}$$
$$\psi_3 = \psi_1 + \frac{4\pi}{3}.$$

Consider now the Coleman Transformation for a three-bladed rotor. For a given degree of freedom q_i in the rotating reference frame, the Coleman Transform is given by

$$\begin{aligned} q_0 &= \frac{1}{3}\sum_{i=1}^{3} q_i \\ q_c &= \frac{2}{3}\sum_{i=1}^{3} q_i \cos\psi_i \\ q_s &= \frac{2}{3}\sum_{i=1}^{3} q_i \sin\psi_i, \end{aligned} \tag{4.27}$$

where

- q_0 is the collective term.
- q_c is the cosine-cyclic term.
- q_s is the sine-cyclic term.

If e.g. q_i is flapwise deflection of the blades, q_0 describes the collective flap of the blades while q_c and q_s describe the tilt and yaw flap motions, respectively.

Transformation from the nonrotating reference frame is done by the inverse transformation given by

$$q_i = q_0 + q_c \cos\psi_i + q_s \sin\psi_i, \quad i = 1, 2, 3. \tag{4.28}$$

With this transformation it is possible to describe the $1P$ asymmetric loads through q_c and q_s. Choosing q_i as the axial blade moment $M_{\mathrm{b,i}}$ it is seen that if q_c and q_s are both zero, the $1P$ asymmetric load on the rotor is also zero under the assumption that the rotor is excited by a wind field without lateral and vertical components. Thus, q_c and q_s describe a cost that the designed controller should aim to reduce. For the Coleman Transformation on M_b, q_c, and q_s will be named the tilt moment M_{tilt} and yaw moment M_{yaw}, respectively. Thus, the transformation becomes

$$\begin{bmatrix} M_{\text{tilt}} \\ M_{\text{yaw}} \end{bmatrix} = T_c \begin{bmatrix} M_{b1} \\ M_{b2} \\ M_{b3} \end{bmatrix}$$
$$T_c = \frac{2}{3} \begin{bmatrix} \cos(\psi_1) & \cos\left(\psi_1 + \frac{2\pi}{3}\right) & \cos\left(\psi_1 + \frac{4\pi}{3}\right) \\ \sin(\psi_1) & \sin\left(\psi_1 + \frac{2\pi}{3}\right) & \sin\left(\psi_1 + \frac{4\pi}{3}\right) \end{bmatrix}, \tag{4.29}$$

where T_c is the Coleman transformation matrix.

4.2.2 Tower Deflection

The thrust force F_T from the rotor is transferred to the structure of the wind turbine. This results in a nonlinear deflection of the tower. A linear approximation of the deflection is used with one degree of freedom, x_t, which corresponds to a translation of the tower in the downwind direction. A mass-spring-damper equivalent is used which is seen in figure 4.7.

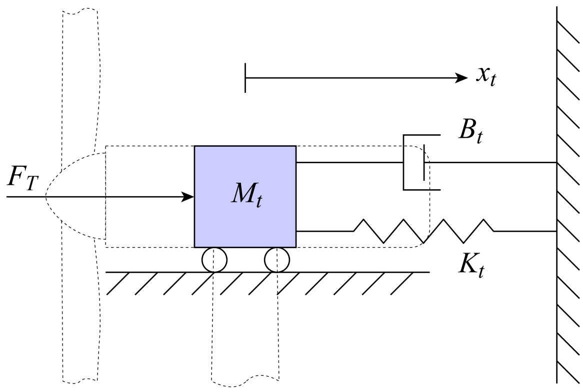

Figure 4.7: Lumped representation of the wind turbine fore-aft tower deflection. The tower deflection x_t is positive in the downwind direction.

Since the thrust force from 4.15 on page 26 is for a single blade, these must be summarized to give the total thrust force F_T:

$$F_T = \sum_{i=1}^{3} F_{T,i} \tag{4.30}$$

The deflection is then given by

$$\ddot{x}_t(t) M_t = F_T(t) - K_t x_t(t) - B_t \dot{x}_t(t), \tag{4.31}$$

where

- M_t is the equivalent mass of the tower [kg].
- B_t is the damping coefficient $[\frac{\mathrm{N\cdot s}}{\mathrm{m}}]$.
- K_t is the stiffness $[\frac{\mathrm{N}}{\mathrm{m}}]$.

It is assumed that the thrust force F_T is the one acting on the tower. This is not correct since some of the force will result in bending of the blades. But because the parameters of the tower deflection equivalent are estimated, this error will be reduced by scaling the parameters accordingly.

4.3 Pitch Actuators

The pitch actuators are modeled as first-order closed-loop systems with constraints on the pitch positions and the maximum pitch rate. The closed-loop system ensures that a given pitch reference is obtained. Figure 4.8 shows the model of the system.

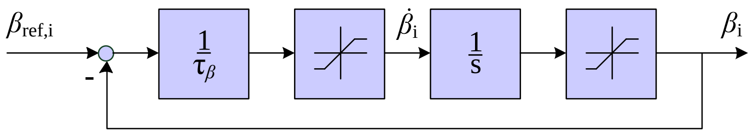

Figure 4.8: Block diagram of the pitch actuator model.

The system is described by the equation

$$\dot{\beta}_i(t) = \frac{1}{\tau_\beta}\left(\beta_{\mathrm{ref,i}}(t) - \beta_i(t)\right), \quad i = 1, 2, 3, \tag{4.32}$$

subject to the constraints

$$\begin{aligned} \beta_{\min} \leq \beta_i(t) \leq \beta_{\max} \\ |\dot{\beta}_i(t)| \leq \beta_{\mathrm{rate}}. \end{aligned} \tag{4.33}$$

where

- τ_β is the time constant of the blade pitch system [s].
- $\beta_{\mathrm{ref,i}}$ is the pitch angle reference for the i'th blade [rad].
- β_i is the pitch angle of the i'th blade [rad].
- $\beta_{\min}$ are the minimum blade pitch angle [rad].
- $\beta_{\max}$ are the maximum blade pitch angle [rad].
- β_{rate} is the maximum pitch rate $[\frac{\mathrm{rad}}{\mathrm{s}}]$.

4.4 Drivetrain

The drivetrain of a wind turbine transfers the rotational torque of the rotor T_r to the generator which in turn transforms it to electrical power by applying a generator torque T_g. The rotational torque of the rotor T_r is given by summation of the contributions from the individual blades from (4.14) by

$$T_r = \sum_{i=1}^{3} T_{r,i}. \tag{4.34}$$

As traditional generators operate at higher rotational speeds than the rotor, a gearing between the rotor and the generator is used. The rotor is mounted on a shaft usually termed the low-speed shaft which connects to the high-speed shaft of the generator through the gearing.

The system is modeled by two inertias: One for the low-speed shaft and one for the high-speed shaft. A rotational damping B_θ and a rotational stiffness K_θ are added to the low-speed shaft to model the shaft torsion θ. Shaft torsion in the high-speed shaft is not considered since this is usually negligible compared to the low-speed shaft torsion. Viscous friction in shaft bearings will also be neglected since they are not incorporated in FAST and thus the 5 MW turbine model. The model of the drivetrain is shown in figure 4.9.

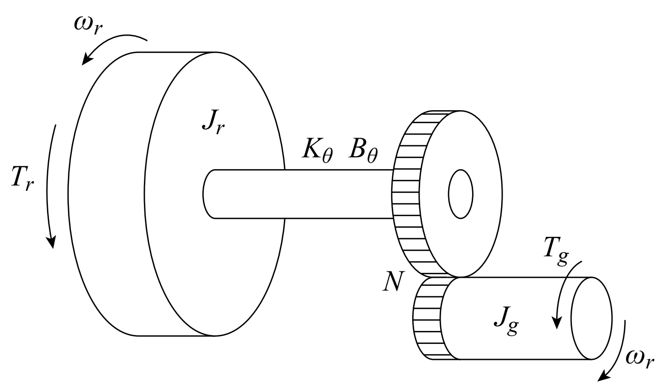

Figure 4.9: Lumped representation of the wind turbine drivetrain dynamics. The angular velocities ω_r and ω_g have opposite positive directions.

The free-body diagram used for deriving the system equations is shown in figure 4.10 on the next page.

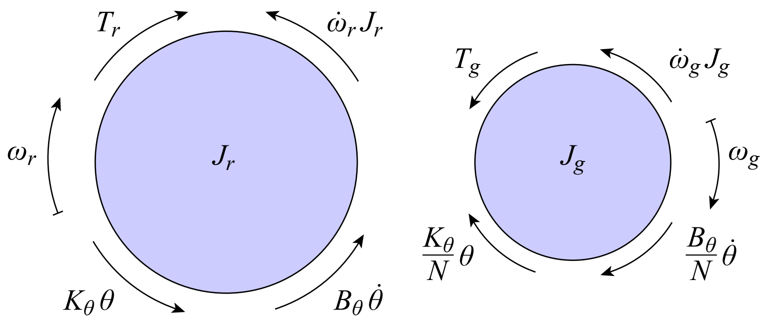

Figure 4.10: Free-body diagram of the drivetrain shafts.

Summing the terms from figure 4.10 and noting the expression for the shaft torsion speed the equations for the system is written as

$$\begin{aligned}
\dot{\omega}_r(t)J_r &= T_r(t) - K_\theta\theta(t) - B_\theta\dot{\theta}(t) \\
\dot{\omega}_g(t)J_g &= -T_g(t) + \frac{K_\theta}{N}\theta(t) + \frac{B_\theta}{N}\dot{\theta}(t) \\
\dot{\theta}(t) &= \omega_r(t) - \frac{\omega_g(t)}{N},
\end{aligned} \tag{4.35}$$

where

- J_r is the moment of inertia of the low-speed shaft [$\mathrm{kg}\cdot\mathrm{m}^2$].
- J_g is the moment of inertia of the high-speed shaft [$\mathrm{kg}\cdot\mathrm{m}^2$].
- θ is the shaft torsion [rad].
- ω_g is the angular velocity of the high-speed shaft [$\frac{\mathrm{rad}}{\mathrm{s}}$].
- K_θ is the rotational stiffness [$\frac{\mathrm{N\cdot m}}{\mathrm{rad}}$].
- B_θ is the rotational damping [$\frac{\mathrm{N\cdot m\cdot s}}{\mathrm{rad}}$].
- N is the gear ratio [$\cdot$].
- T_g is the applied generator torque [$\mathrm{N}\cdot\mathrm{m}$].

4.5 Generator

The generator transforms the rotational speed of the high-speed shaft into power. In Double Fed Induction Generators (DFIG), which are widely used for wind turbines, the generator torque is controlled by changing the current in the rotor of the generator. For the purpose of controlling the wind turbine, the simplifying assumption that the generator torque can be controlled directly will be used. Taking energy conversion efficiency into account, the electric power is described by the nonlinear equation

$$P_e(t) = T_g(t)\omega_g(t)\eta_g, \tag{4.36}$$

where

- η_g is the energy conversion efficiency of the generator $[\cdot]$.
- P_e is the produced electrical power [W].

Constraints are added to the generator torque input. These are given by

$$\begin{aligned} T_{\text{gmin}} \leq T_g(t) &\leq T_{\text{gmax}} \\ |\dot{T}_g(t)| &\leq T_{\text{grate}}, \end{aligned} \tag{4.37}$$

where

- T_{gmin} is the minimum generator torque $[\mathrm{N} \cdot \mathrm{m}]$.
- T_{gmax} is the maximum generator torque $[\mathrm{N} \cdot \mathrm{m}]$.
- T_{grate} is the maximum rate of change of the generator torque $[\frac{\mathrm{N \cdot m}}{\mathrm{s}}]$.

4.6 Linearization

The models of the subsystems constitute a nonlinear state-space model

$$\begin{aligned} \dot{x}_n &= f(x_n, u_n, d_n) \\ z_n &= h(x_n, u_n, d_n), \end{aligned}$$

where

- x_n is the state vector.
- u_n is the control input vector.
- d_n is the disturbance vector.
- z_n is the control output vector.

A model for measurements is not included since a state observer is not developed in this project. It will instead be assumed that full state information is available.

The nonlinear system equations must be linearized since linear Model Predictive Control is used. The following sections describe the variables that are included in the system vectors, the different methods used for linearization, and how the operating points for the linearization have been chosen. Finally, a linear state space representation of the system will be presented.

4.6.1 Identifying Inputs, Outputs, States, and Disturbances

In order to represent the system equations as a linear state space system, the structure of the vectors needs to be identified. The state vector is constructed using the dynamic variables of the system, i.e.

$$x_n = \begin{bmatrix} x_t \\ \dot{x}_t \\ \omega_r \\ \omega_g \\ \theta \\ \beta_1 \\ \beta_2 \\ \beta_3 \end{bmatrix}. \tag{4.38}$$

The control input vector consists of the reference input to the pitch actuator and the torque input to the generator. It is given by

$$u_n = \begin{bmatrix} \beta_{\text{ref1}} \\ \beta_{\text{ref2}} \\ \beta_{\text{ref3}} \\ T_g \end{bmatrix}. \tag{4.39}$$

The disturbance vector consists of the uncontrollable inputs to the system. For this model the three wind inputs to the blades are the uncontrollable inputs and the disturbance vector is therefore given by

$$d_n = \begin{bmatrix} V_1 \\ V_2 \\ V_3 \end{bmatrix}. \tag{4.40}$$

Finally, the control outputs are chosen based on the tuning of the controller. These are the variables that must stay close to a certain reference such as the operating point. The control outputs are

$$z_n = \begin{bmatrix} P_e \\ \beta_1 \\ \beta_2 \\ \beta_3 \\ \dot{\beta}_1 \\ \dot{\beta}_2 \\ \dot{\beta}_3 \\ \dot{x}_t \\ \omega_r \\ \dot{\theta} \\ M_{b1} \\ M_{b2} \\ M_{b3} \end{bmatrix}. \tag{4.41}$$

As seen, the axial blade moment M_b is defined in the rotating reference frame in the control outputs. The transformation of these to tilt and yaw moments happens with the weighting matrix used for the controller. This is described in more detail in chapter 5 on page 45.

4.6.2 Choosing Operating Points

All of the operating points for the model can be determined by the wind speed operating point $\bar{V}_0$, since the wind speed determines the region of operation. Each region has different requirements for the operating point and the task of finding operating points is different for each region. The operating points for the pitch angles are all chosen as one operating point denoted $\bar{\beta}$.

Region 1

In region 1 the goal is to maximize power production. This is achieved by maximizing (4.9) and since $\bar{V}_0$ is determined the only variables left are the pitch angle β and tip speed ratio λ. The maximization problem is written as

$$\begin{aligned} \underset{\beta,\lambda}{\text{maximize}} \quad & P_e(\beta, \lambda, \bar{V}_0) \\ \text{subject to} \quad & 0 \leq \beta_i \leq 90^\circ,\ i = 1, 2, 3 \\ & 6.9 \text{ rpm} \leq \omega_\text{r}, \end{aligned}$$

where the cut-in rotor speed is 6.9 rpm for the NREL 5 MW wind turbine.

Normally in region 1 the pitch is not adjusted and is set to 0 since normally this is where the wind turbine yields the greatest power, thus leaving the generator torque as the only controlled input to the wind turbine.

Region 2

The goal of region 2 is the same as in region 1 except the rotor speed has to be limited. For the NREL 5 MW wind turbine the rated rotor speed is 12.1 rpm.

Region 3

In region 3 the power is at the rated level (5MW) and the rotor speed is fixed at the rated level (12.1 rpm). The operating points for a given wind speed are found by first calculating the tip speed ratio λ. The tip speed ratio is then used along with the C_P-curve, as shown in appendix C on page 77, multiplied by the generator efficiency to find the pitch angle β that achieves the goal of 5 MW produced power.

Operating points

With the tip speed ratio and the pitch angle operating points known $\bar{T}_g, \bar{x}_t, \bar{\omega}_g$, and $\bar{\theta}$ are found by solving

$$f(x_n, u_n, d_n) = 0. \tag{4.42}$$

The operating points $\bar{T}_r, \bar{M}_b$, and $\bar{F}_t$ are found by inserting $\bar{\omega}_r, \bar{\beta}$, and $\bar{V}$ into (4.14)-(4.15).

4.6.3 Methods of Linearization

The only nonlinearities in the system are the aerodynamics and the power output from the generator. Different methods have been used to linearize these. The methods for linearizing these are presented in this section.

Linearizing the Power Output

Equation (4.36) for the power output is linearized using the first-order Taylor series

$$f(\bar{x} + x^{\Delta}) \approx f(\bar{x}) + \frac{\partial f(x)}{\partial x}_{|x=\bar{x}} x^{\Delta}, \tag{4.43}$$

where

- $\bar{x}$ is the operating point.

- x^{Δ} is a pertubation from the operating point.

Using the taylor series on the power output equation and subtracting the operating point from the equation the linear equation becomes

$$P_e^{\Delta}(t) = \eta_g \bar{\omega}_g T_g^{\Delta}(t) + \eta_g \bar{T}_g \omega_g^{\Delta}(t), \tag{4.44}$$

Linearizing the Aerodynamics

Since the aerodynamics are found numerically, the Taylor series can not be used to linearize these. The aerodynamics are therefore also linearized numerically.

The blade equations (4.14), (4.16), and (4.15) can all be parametized by V_w, ω_r, and β_i. For an operating point given by $\bar{V}_0$ it is desired to obtain a coefficient matrix as

$$\begin{bmatrix} T_{\mathrm{r,i}}^{\Delta} \\ M_{\mathrm{b,i}}^{\Delta} \\ F_{\mathrm{t,i}}^{\Delta} \end{bmatrix} = \begin{bmatrix} C_{11} & C_{12} & C_{13} \\ C_{21} & C_{22} & C_{23} \\ C_{31} & C_{32} & C_{33} \end{bmatrix} \begin{bmatrix} V_w^{\Delta} \\ \omega_r^{\Delta} \\ \beta_i^{\Delta} \end{bmatrix} \tag{4.45}$$

The coefficients are found by making small pertubations from the operating points of V_w, ω_r, and β. E.g. C_{11} is obtained by

$$C_{11} = \frac{T_r(\bar{V}_w + \Delta V_w, \bar{\omega}_r, \bar{\beta}) - T_r(\bar{V}_w - \Delta V_w, \bar{\omega}_r, \bar{\beta})}{2\Delta V_w} \tag{4.46}$$

where ΔV_w is a small pertubation added and subtracted from the operating point. It should be noted that $\bar{V}_w = \bar{V}_0$.

Similarly for the second and third column, pertubations from $\bar{\omega}_r$ and $\bar{\beta}$ are made while the other parameters are kept at the operating point.

4.6.4 State Space Representation

With the nonlinear parts of the model now linearized, it is possible to represent the model as a linear state space system. As the linearized equations now describe pertubations from the operating point, the rest of the model must also be transformed this way. Therefore, the operating point is subtracted as

$$\begin{aligned} x &= x_n - \bar{x}_n \\ u &= u_n - \bar{u}_n \\ d &= d_n - \bar{d}_n \end{aligned} \tag{4.47}$$

where x, u, and d are the pertubation vectors. z will denote the control outputs for the linearized model.

The system matrices can all be parametized by the operating point for the freestream wind speed denoted by $\bar{V}_0$. Using the method from section 4.6.2 on page 36, the rest of the operating points can be found using only $\bar{V}_0$. The linear state space model is written as

$$\begin{aligned} \dot{x} &= A(\bar{V}_0)x + B_u(\bar{V}_0)u + B_d(\bar{V}_0)d \\ z &= C(\bar{V}_0)x + D_u(\bar{V}_0)u + D_d(\bar{V}_0)d \end{aligned} \tag{4.48}$$

The model is prepared for the controller by a discretization using a zero-order hold approximation with a sampling time of 0.1 seconds, which more than twice as fast as the fastest natural frequency of the system (3.2 Hz).

4.7 Model Parameters and Verification

The parameters for the model are primarily found using the definition document of the NREL 5 MW turbine (Jonkman et al., 2009). Some of the parameters for the electrical generator and the pitch actuator are however not defined for the NREL 5 MW turbine. Therefore it has been chosen to use the parameters from the Aeolus project for electrical generator energy conversion efficiency and for the pitch actuator time constant. The parameters for tower structure model are based on the natural frequency and the damping-ratio of tower. The stiffness, mass, and damping coefficients are then found using the known natural frequency and damping-ratio. Appendix B on page 75 shows the parameters of the model.

4.7.1 Verification

In order to use the model for control purposes it has to be verified. The verification has been done for a model linearized at 18 m/s, as this is the mean speed for tests performed for the controllers. Four different outputs are shown (Rotor speed, shaft torsion, tower bending, and axial blade moments) of the verified states. The input for the verification is a series of step in the wind as seen in figure 4.11 on the next page, except for the verification of the axial bending moments, where a wind field with mean 18 m/s has been generated with TurbSim (Jonkman, 2009). The wind field used for the wind steps has the same wind speed at all points in the rotor plane. Both time series and Power Spectral Densitites (PSD) are shown for each comparison.

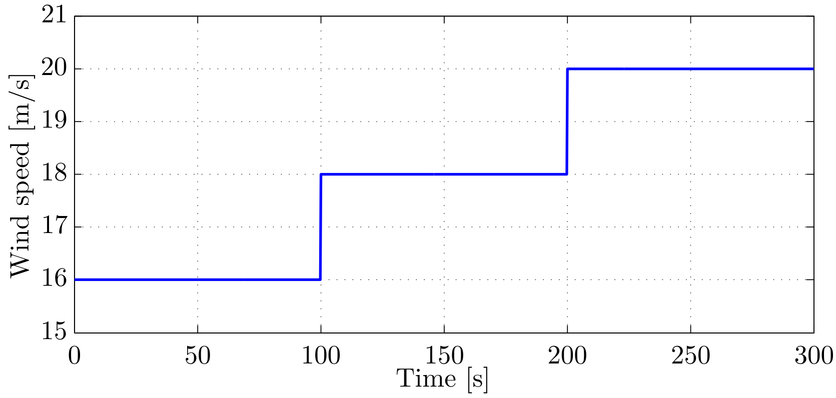

Figure 4.11: Steps in wind speed for the verification.

For the rotor speed model it is very important that it has a low steady state error since it is used to establish the operating points for the linearized model. As seen in figure 4.12, the rotor speed for the linearized model is very similar to FAST for both the steady state and the dynamics. The PSD is also calculated and is shown in figure 4.13 on the next page, which shows that the model is very similar to FAST. This is no surprise since FAST uses the same parameters. Since there is a low steady state error and the dynamics are similar, it indicates that the model is not very sensitive to changes in mean wind regarding the rotor speed.

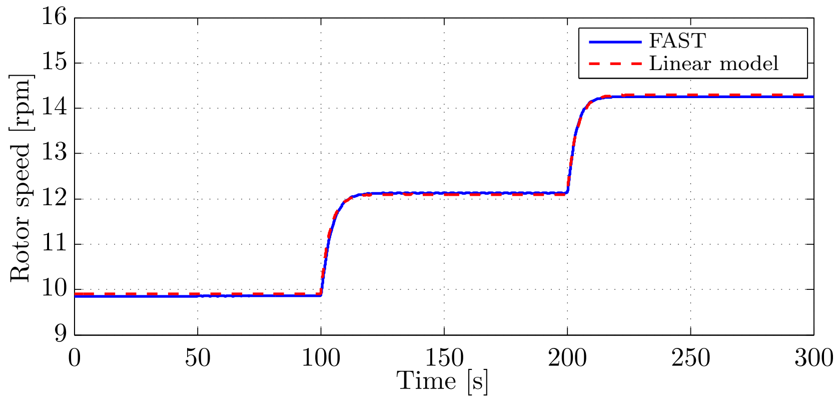

Figure 4.12: Rotor speed for FAST and the linear model linearized at 18 m/s.

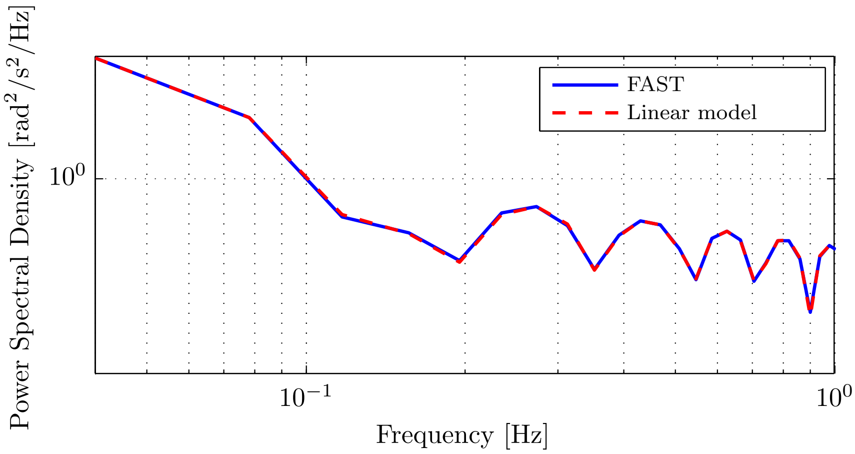

Figure 4.13: PSD of the rotor speed for both FAST and the linearized model.

The torsion of the low-speed shaft for both FAST and the linearized model is shown in figure 4.14, where it is seen that the linearized model seems to have a lower damping ratio than that of FAST. However since the shaft torsion is very sensitive to small changes in the rotor speed, and there are unmodeled dynamics may contribute to the inaccuracies. It is therefore very difficult to look at the shaft torsion isolated from the rest of the FAST model. Figure 4.15 on the next page shows that they have slightly different peaks. The model of the shaft torsion is sufficient to be used for control purposes, since it captures the tendencies

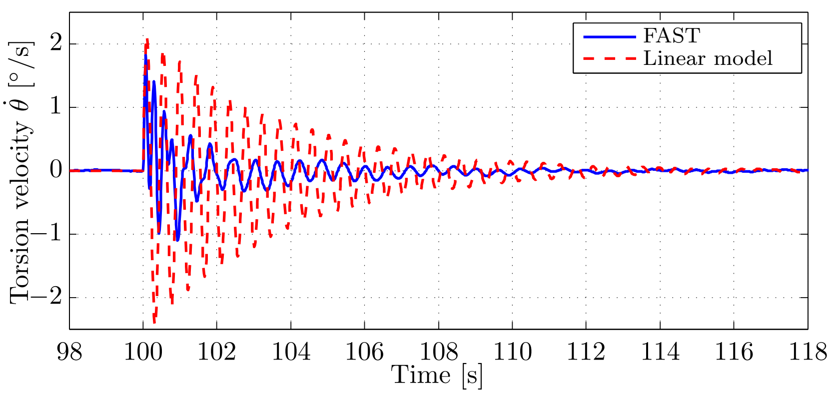

Figure 4.14: Shaft torsion for FAST and the linear model linearized at 18 m/s.

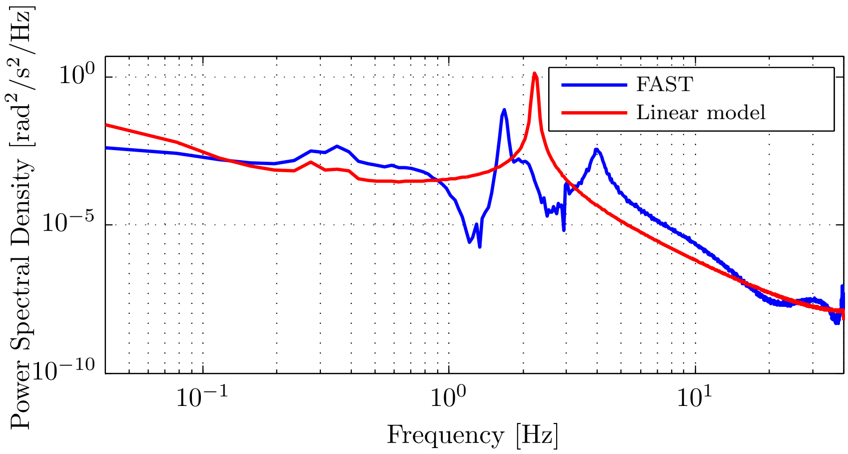

Figure 4.15: PSD of the shaft torsion for both FAST and the linear model linearized at 18 m/s.

The tower oscillations caused by steps in wind speed are shown in figure 4.16. FAST and the linearized model are very similar and the PSD, as shown in figure 4.17 on the next page, shows aswell that the linearized model is very accurate. It is chosen to use a simple wind field for the verification of the tower bending to isolate the tower dynamics from the unmodeled dynamics. As with the rotor model the linearized tower structure model uses the same parameters as FAST.

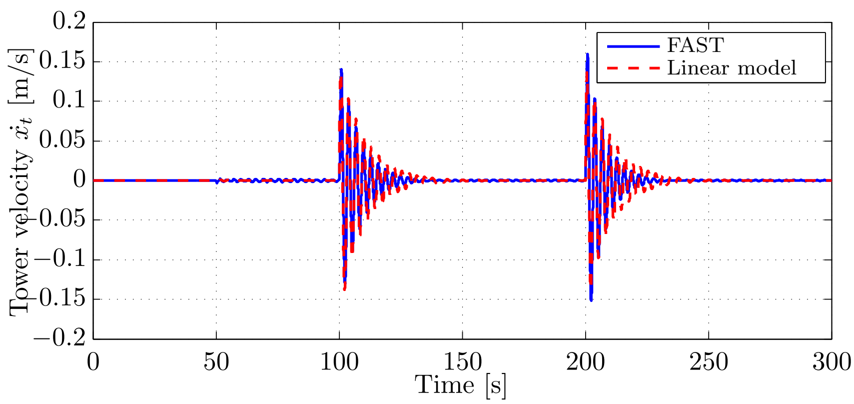

Figure 4.16: Fore-aft tower deflection for FAST and the linear model linearized at 18 m/s.

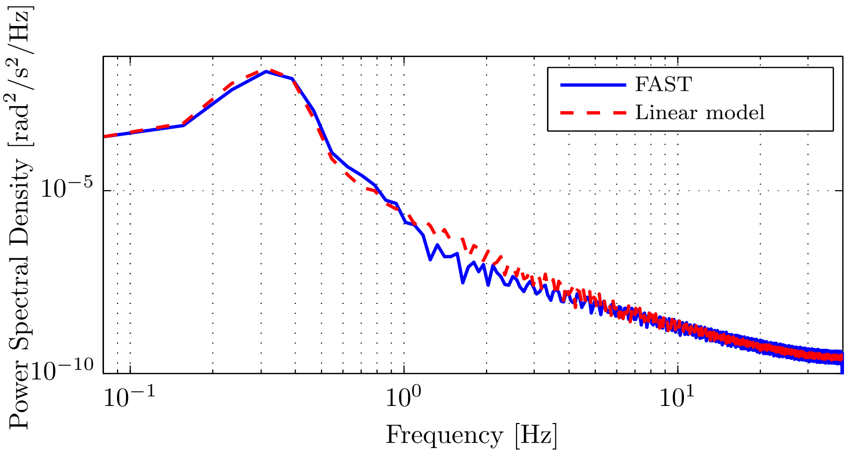

Figure 4.17: PSD of the tower bending for both FAST and the linear model linearized at 18 m/s.

The axial blade moments of the blades play a key role in this project as the goal is to reduce asymmetric loads. In comparison of axial blade moments it is chosen to use a stochastic wind field with 18 m/s mean wind speed to excite the blades, since the steps in wind do not provide sufficient excitation of the blades. The comparison of FAST and the linearized model, for the axial blade moments of a blade, is shown in figure 4.18. The linearized model seems to be similar to FAST. The PSD is shown in figure 4.19 on the next page and shows that the linearized model is accurate. Furthermore a peak at approximately 0.2 Hz is observed, which is the $1P$ frequency.

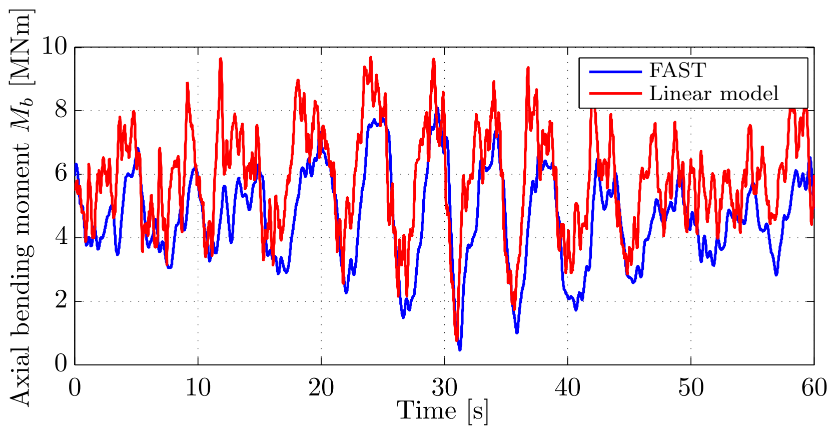

Figure 4.18: Axial blade moments of a single blade for FAST and the linear model linearized at 18 m/s.

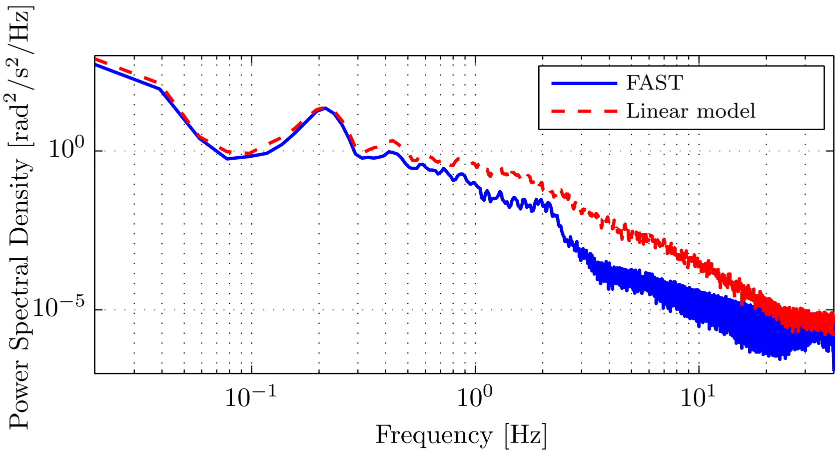

Figure 4.19: PSD of the axial blade moments of a single blade for both FAST and the linearized model.

The linearized model seems to be a good estimate of FAST except for the torsion which is difficult to isolate.

Chapter 5

Predictive Control

The goal of this project is to keep the power at a reference in region 3 while reducing the asymmetric loads in the structure caused by an asymmetric wind field. Other loads are shaft torsion and tower deflection. Activity of the actuators is also a concern and constraints of actuators must not be violated. Since the LIDAR is used the controller must also be able to handle preview measurements as well.

In this project it is chosen to use Model Predictive Control (MPC) to handle the requirements to the control of the wind turbine. Model Predictive Control (MPC) is an online nonlinear control scheme based on a linear model and not to be confused with nonlinear MPC (NMPC) which is based on a nonlinear model. MPC is well suited for systems with constraints and preview measurements which standard linear control has difficulties dealing with. MPC estimates future states of the system by using a model of the system and often a linear model is used. These estimates are then weighted in the cost function of the MPC over a given horizon and an optimal input series is computed subject to a given set of constraints. The first input of the input series is then aplied to the system. This proces is then repeated for each time step.

The iterative nature of the MPC enables it to handle constraints, and the cost function can easily handle preview measurements. MPC is classified as an online nonlinear control scheme, thus it is not as trivial to guarantee stability in contrary to ordinary linear control. However there are several techniques to guarantee stability. The implementation of MPC can be done in several different ways depending on the problem. Since the controller is an online optimization problem it is usually necessary to take the sampling time into account in order to give the optimization algorithm time to calculate an input. Another way to implement the MPC is to use precomputed lookup tables which is faster though only applicable for smaller problems (Maciejowski, 2000).

In this chapter it is shown how the linear model and LIDAR is used with MPC in section 5.1, the control formulation of MPC on the wind turbine will be presented in section 5.2, in section 5.3 on page 52 the tuning and implementation of the controller is presented, and in section 5.4 on page 53 stability and feasibility of the MPC is adressed. Most of the notation and equations in this section is based on the work in (Maciejowski, 2000).

5.1 Using the Model and LIDAR for MPC

As already mentioned a model is needed for MPC, and preview measurements are provided by the LIDAR. A linear model is used as described in section 4.6 on page 34 with the outputs z. The linear model is linearized at 18 m/s because the tests performed in chapter 6 on page 55 are made with a 18 m/s mean wind. The asymmetric loads (M_{tilt} and M_{yaw}) are highly dependent of the azimuth angle. The transformation of those so they can be used in the controller is dealt with in section 5.2.3 on page 51 by transforming the axial blade moments M_b of each blade via the Coleman transformation as seen in section 4.2.1 on page 28.

In order to reduce the asymmetric loads LIDAR is used. The LIDAR provides preview measurements of the wind field ahead of the wind turbine. A fixed distance D is chosen (54 m) as seen in section 3 on page 13. The LIDAR measurements are stored in a queue, which contains the measured data for the last 3 seconds.

5.2 Problem Formulation

MPC consists of roughly two parts: a cost function and a set of constraints. In traditional MPC the cost function is a quadratic function and the constraints are linear inequalities. This is however not a necessity. The cost function can be any mathematical expression depending on the goal of the control. However to secure a global solution of the problem it is necessary to have a convex problem formulation.

In this project a standard quadratic function is chosen to keep the problem formulation simple. Furthermore the quadratic cost function yields a simple way of introducing the asymmetric loads as seen in section 5.2.3 on page 51. The constraints are simple linear limit constraints in the actuators.

As stated in chapter 4 on page 19 the wind turbine is mounted with a LIDAR to measure wind data ahead of the wind turbine. In this section MPC for this project is presented and schematic of the controller is shown in figure 5.1 on the next page, where it is seen that controller gets the state information directly from FAST and the LIDAR data is stored in the queue. Since the controller is run on a simulator no considerations regarding the computational delay from the MPC.

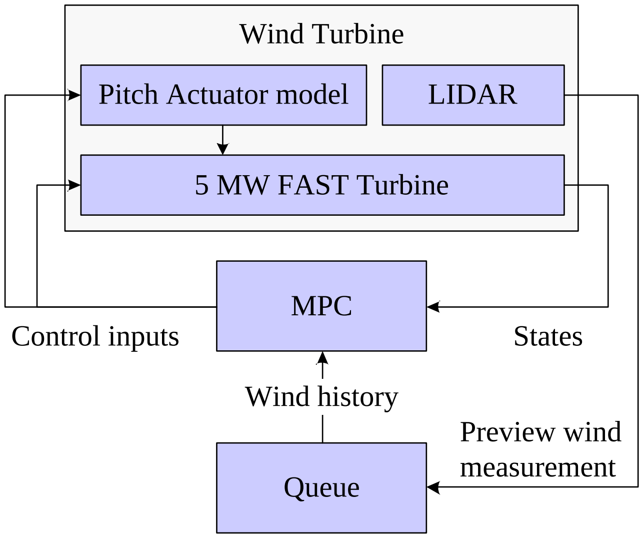

Figure 5.1: Schematic of the controller.

5.2.1 Cost function

The quadratic cost function at time step k weights both outputs and inputs over their respective horizons and is expressed as

$$
\begin{aligned}
J_z(k) &= \sum_{i=0}^{H_p} \|\hat{z}(k+i|k) - r(k+i)\|_Q^2 \\
J_{\Delta u}(k) &= \sum_{i=0}^{H_u-1} \|\Delta\hat{u}(k+i|k)\|_R^2 \\
J(k) &= J_z(k) + J_{\Delta u}(k),
\end{aligned}
\tag{5.1}
$$

where

- H_p is the prediction horizon.
- H_u is the control horizon.
- Q is the output weighting matrix.
- R is the input weighting matrix.
- $\Delta\hat{u}$ are control moves.

- r is reference to the controller.
- J_z is the cost of the estimated outputs over the prediction horizon given the output weighting matrix Q.
- $J_{\Delta u}$ is the cost of the change in input over the input horizon given the input weighting matrix R.
- J is the total cost.

Since the model is linearized around operating points, the reference r is always 0 for all of the outputs, thus r is omitted.

Δu notation

Often MPC is formulated in a way so the input to the system is given in terms of control moves Δu, as seen in (5.1), instead of the normal input u. This is also the case for this project which means that a slight reformulation of the model is needed. The control moves Δu are given by

$$\Delta u(k) = u(k) - u(k-1). \tag{5.2}$$

The linearized state-space model is given by (4.48) is transformed to the Δu notation by

$$\mathcal{Z}(k) = \Psi x(k) + \Upsilon u(k-1) + \Theta \Delta \mathcal{U} + \Xi \mathcal{D}(k), \tag{5.3}$$

where

- $\mathcal{Z}(k)$ are the outputs over the prediction horizon H_p represented as vector.
- $\Delta\mathcal{U}(k)$ are the control moves over the control horizon H_u represented as a vector.
- $\mathcal{D}$ are the measured disturbancies over the prediction horizon H_p represented as a vector.

The vector representation of $\mathcal{Z}(k)$, $\Delta\mathcal{U}(k)$, and $\mathcal{D}$ are given by

$$\mathcal{Z}(k) = \begin{bmatrix} \hat{z}(k|k) \\ \vdots \\ \hat{z}(k+H_p|k) \end{bmatrix}, \Delta\mathcal{U}(k) = \begin{bmatrix} \Delta\hat{u}(k|k) \\ \vdots \\ \Delta\hat{u}(k+H_u-1|k) \end{bmatrix}, \mathcal{D}(k) = \begin{bmatrix} d(k) \\ \vdots \\ d(k+H_p-1) \end{bmatrix}.$$

The matrices Ψ, Υ, Θ, and Ξ are given by

$$\Psi = \begin{bmatrix} CA \\ CA^2 \\ \vdots \\ CA^{H_p} \end{bmatrix}, \tag{5.4}$$

$$\Upsilon = \begin{bmatrix} CB_u + D_u \\ CAB_u + D_u \\ \vdots \\ C\sum_{i=0}^{H_p-1} A^i B_u + D_u \end{bmatrix}, \tag{5.5}$$

$$\Theta = \begin{bmatrix} CB_u & 0 & \cdots & 0 \\ CAB_u + CB_u + D_u & CB_u & \cdots & 0 \\ \vdots & \vdots & \ddots & \vdots \\ C\sum_{i=0}^{H_p-1}(A^i B_u) + D_u & C\sum_{i=0}^{H_p-2}(A^i B_u) + D_u & \cdots & C\sum_{i=0}^{H_p-H_u} A^i B_u \end{bmatrix}, \tag{5.6}$$

$$\Xi = \begin{bmatrix} CB_d + D_d & 0 & \cdots & 0 \\ CAB_d & CB_d + D_d & \cdots & 0 \\ \vdots & \vdots & \ddots & \vdots \\ CA^{H_p-1}B_d & CA^{H_p-2} & \cdots & CB_d + D_d \end{bmatrix}. \tag{5.7}$$

With the tranformation to Δu notation it is now possible to represent the cost function as

$$\begin{aligned} J(k) &= \mathcal{Z}(k)^T Q \mathcal{Z}(k) + \Delta\mathcal{U}(k)^T R \Delta\mathcal{U} \\ &= (\mathcal{C} + \Theta\Delta\mathcal{U}^T) Q (\mathcal{C} + \Theta\Delta\mathcal{U}) + \Delta\mathcal{U}(k)^T R \Delta\mathcal{U} \\ &= \mathcal{C}^T\mathcal{C} + \Delta\mathcal{U} 2\Theta Q \mathcal{C} + \Delta\mathcal{U}(k)^T(\Theta^T Q \Theta + R)\Delta\mathcal{U} \end{aligned} \tag{5.8}$$

where $\mathcal{C} = \Psi x(k) + \Upsilon u(k-1) + \Xi\mathcal{D}$ and is independent from decision variables.

5.2.2 Constraints

It is possible to have three different types of constraints: input changes, inputs, and outputs. The constraints can change over the respective horizons and can be different at each time step. This is however not the case in this project, since the only constraints considered are actuator constraints which do not change over the control horizon nor change over time.

In this project all three types of constraints are present. The generator rate constraints are represented in the control moves constraint matrix E, the limits on the generator torque are represented in the input constraint matrix G, the pitch actuator constraints are represented in the output constraint matrix L. The last column of E, G, and L contain the limits on the variable, the remaining columns contain information of which variables belong to which limits at which times. The constraints are shown in (5.9).

$$E \begin{bmatrix} \Delta\mathcal{U}(k) \\ 1 \end{bmatrix} \leq 0, G \begin{bmatrix} \mathcal{U}(k) \\ 1 \end{bmatrix} \leq 0, L \begin{bmatrix} \mathcal{Z}(k) \\ 1 \end{bmatrix} \leq 0 \tag{5.9}$$

As stated earlier, the MPC problem is formulated in Δu notation. The constraints must therefore be transformed to only be dependent on Δu. Only the input constraints and output constraints need to be reformulated since the input moves constraints already are in the correct form. The input contraints are transformed by

$$\mathcal{G}\Delta\mathcal{U}(k) \leq -\mathcal{G}_1 u(k-1) - g, \tag{5.10}$$

where $\mathcal{G}_j$ is the j'th column of $\mathcal{G}$. The matrix $\mathcal{G}$ acts an integration of the columns of G. $\mathcal{G}$ is given by

$$\mathcal{G} = \begin{bmatrix} \sum_{j=1}^{H_u} G_j & \sum_{j=2}^{H_u} G_j & \cdots & G_{H_u} \end{bmatrix}, \tag{5.11}$$

G_j is the j'th column of G and g is the last column of G. The output constraints are transformed by combining the expression for the output constraints from (5.9) with the expression for $\mathcal{Z}(k)$ from (5.3) as

$$L \begin{bmatrix} \Psi x(k) + \Upsilon u(k-1) + \Theta\Delta\mathcal{U} + \Xi\mathcal{D}(k) \\ 1 \end{bmatrix} \leq 0, \tag{5.12}$$

and reduced to

$$\Gamma\Theta\Delta\mathcal{U} \leq -\Gamma(\Psi x(k) + \Upsilon u(k-1) + \Xi\mathcal{D}(k)) - l, \tag{5.13}$$

where $L = [\Gamma, l]$ with l being the last column of L and Γ represents the rest of the columns. With all the constraints transformed they can described as

$$\begin{bmatrix} \mathcal{G} \\ \Gamma\Theta \\ \Lambda \end{bmatrix} \Delta\mathcal{U} \leq \begin{bmatrix} -\mathcal{G}_1 u(k-1) - g \\ -\Gamma(\Psi x(k) + \Upsilon u(k-1) + \Xi\mathcal{D}(k)) - g \\ -e \end{bmatrix}, \tag{5.14}$$

where E is partitioned as $E = [\Lambda, e]$ with e being the last column of E and Λ represents the rest of the columns.

5.2.3 Transformation of the Axial Blade Moments

The yaw and tilt moments are nonlinear with respect to the azimuth angle, as shown in (4.29) and can not be used as outputs of the linear model without scheduling very frequently. Instead they are introduced through the output weighting matrix Q. As the cost function is quadratic, the tilt and yaw moments must be defined as quadratic terms as well. In other words the goal is to reduce $M_{\text{tilt}}^2 + M_{\text{yaw}}^2$. It is still necessary to maintain positive semi-definitiness in order to secure a global solution of the problem.

Squaring the expression for M_{tilt} from (4.29) yields

$$\begin{aligned} M_{\text{tilt}}^2 = \frac{2^2}{3^2} \Bigg(&\cos(\psi)^2 M_{b1}^2 + \cos\left(\psi + \frac{2\pi}{3}\right)^2 M_{b2}^2 + \cos\left(\psi + \frac{4\pi}{3}\right)^2 M_{b3}^2 \\ &+ 2\cos(\psi)\cos\left(\psi + \frac{2\pi}{3}\right) M_{b1}M_{b2} + 2\cos(\psi)\cos\left(\psi + \frac{4\pi}{3}\right) M_{b1}M_{b3} \\ &+ 2\cos\left(\psi + \frac{2\pi}{3}\right)\cos\left(\psi + \frac{4\pi}{3}\right) M_{b2}M_{b3} \Bigg). \end{aligned} \tag{5.15}$$

The same can be done for M_{yaw}. Combining the expression for M_{tilt}^2 and M_{yaw}^2 and using matrix notation yields

$$M_{\text{tilt}}^2 + M_{\text{yaw}}^2 = \begin{bmatrix} M_{b1} & M_{b2} & M_{b3} \end{bmatrix} \mathcal{T} \begin{bmatrix} M_{b1} \\ M_{b2} \\ M_{b3} \end{bmatrix}, \tag{5.16}$$

where $\mathcal{T} = T_c^T T_c$, thus making it positive semidefinite, since by definition a matrix multiplied by its transpose is always positive semidefinite. By using the following trigonometric identities

$$\cos(x)^2 + \sin(x)^2 = 1 \tag{5.17}$$

$$\cos(x - y) = \cos(x)\cos(y) + \sin(x)\sin(y), \tag{5.18}$$

the matrix $\mathcal{T}$ is reduced to

$$\mathcal{T} = \frac{2^2}{3^2}\begin{bmatrix} 1 & -\frac{1}{2} & -\frac{1}{2} \\ -\frac{1}{2} & 1 & -\frac{1}{2} \\ -\frac{1}{2} & -\frac{1}{2} & 1 \end{bmatrix}, \tag{5.19}$$

which also shot that $\mathcal{T}$ is positive semidefinite with eigenvalues $[0, 1.5, 1.5]$. Furthermore $\mathcal{T}$ is constant and independent from ψ. The output weighting matrix Q is now expressed as

$$Q = \begin{bmatrix} \mathrm{I} & 0 \\ 0 & \mathcal{T} \end{bmatrix} Q_w, \tag{5.20}$$

where I is the identity matrix and Q_w is a diagonal matrix containing the weights of each output. The squared tilt and yaw moments are now included in the cost function and are independent from ψ which makes the MPC problem less complicated since a prediction of ψ is not needed to generate output weighting matrices for each time step in the prediction horizon. Instead Q is constant over the entire prediction horizon and is positive semidefinite, thus making sure there is a global minimum.

5.3 Implementation

The controller is implemented in Simulink as an S-function with a sample frequency of 10 Hz, which is faster than the highest natural frequency of the system (3.2 Hz). No considerations regarding real-time has been done as the goal is merely to show the possibilities of using LIDAR. The MPC optimization problem is solved using the Matlab function `quadprog`, which is function for solving constrained quadratic problems. The tuning parameters of the controller are H_p, H_u, Q_w and R. The prediction horizon H_p is set to 15 (1.5 seconds) and the control horizon H_u is at 5 (0.5 seconds). Two controllers are designed, to see the effect of LIDAR: one with LIDAR and one without. The controller designed with LIDAR is a individual pitch controller using tilt and yaw moments, and the other is a collective pitch controller. The weightings Q_w and R are diagonal matrices with the weights as listed in table 5.1 on the facing page.

Weights		
	With LIDAR	**Without LIDAR**
P_e	1000	1000
$\dot{\beta}$	1E6	1E6
$\dot{x}_t$	200	200
$\dot{\theta}$	5	5
$M_{\text{tilt}}/M_{\text{yaw}}$	2E-12	-
β	1	5
ω_r	5000	5000
T_g	1E-6	1E-6

Table 5.1: Table of the weights used in the MPCs with and without LIDAR respectively.

The reason there is a difference in the pitch angle weight is that the controller without LIDAR is a collective pitch controller, and thus a higher gain is needed. The controller is as stated implemented in Simulink as a controller for the NREL 5 MW wind turbine in FAST. The measurements used for the controller are provided by FAST and no observer or filtering of the measurements is used.

5.4 Feasibility and Stability

In this project no stability considerations have been made because the gfocus of this project is to show the capabilities of MPC with LIDAR applied to wind turbines. However, if implemented on a real wind turbine stability of the closed-loop system is critical. To secure stability of MPC terminal contraints could be used. This can however make the optimiaztion problem infeasible due to the introduction of constrained outputs. The hard constraints can be softened to make the controller feasible. Another approach is to have a high terminal weight instead of a terminal constraint. This however does not guarantee stability but can help greatly.

The controller is designed with no constraints on the output except the pitch angle and the pitch rate since the pitch angle is a state. However the pitch system is an isolated system and is undisturbed. This results in an optimization problem that is always feasible, thus no further feasiblity considerations are made.

Chapter 6

Results

As already mentioned in chapter 5 on page 45 two MPCs were designed with the only difference that one is designed with LIDAR integration and the other is not. The controller designed with LIDAR is an individual pitch controller and the controller without LIDAR is a collective pitch controller. In addition to the MPCs another controller is introduced to compare them to a standard way of controlling a wind turbine. This controller is the NREL Baseline controller for the NREL 5 MW wind turbine as seen in section 2.4.2 on page 11. The baseline controller is a gain scheduled collective pitch controller.

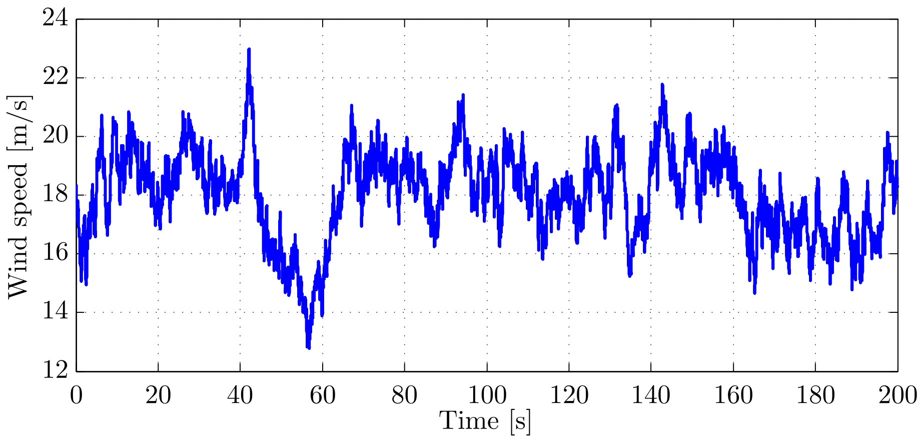

Figure 6.1: Wind speed at the hub.

The tests performed in this chapter are done for a wind field with 18 m/s mean wind speed generated by TurbSim (Jonkman, 2009), as shown in figure 6.1 for the hub wind speed, which is different from the wind field used for tuning the MPCs. The tests run for 200 seconds with the startup of the wind turbine cut off. The linear model used for the MPCs is linearized at 18 m/s and no scheduling is performed.

Only full load operation is tested, so all controllers are designed for region 3 control. During the tests full state information is assumed and are obtained from FAST.

The goal of all the controllers is to maintain a given power level (5 MW) since the wind turbine is operating in region 3. The loads considered for the results are: Fore-aft tower deflection, low-speed shaft torsion, flapwise blade bending moment, edgewise blade bending moment, low-speed shaft tip bending moment in the non-rotating reference frame, and low-speed shaft tip bending moment in the rotating reference frame. Furthermore the actuator signals are also compared to see if the reductions are achieved with reasonable actuator movement. For all the loads both the time series and Power Spectral Density (PSD) are shown. Some of the time series are focused at smaller time intervals to show the characteristics of the signal.

The main goal is to produce power and produce a good power quality. Figure 6.2 shows the power production of each of the three controllers. No significant difference between the controllers is observed except at around 60 s where the controllers without LIDAR deviates a bit from the 5 MW. This is due to a huge change in wind speed as seen in figure 6.1 on the preceding page. The PSD of the power production shows similar performance of the controllers.

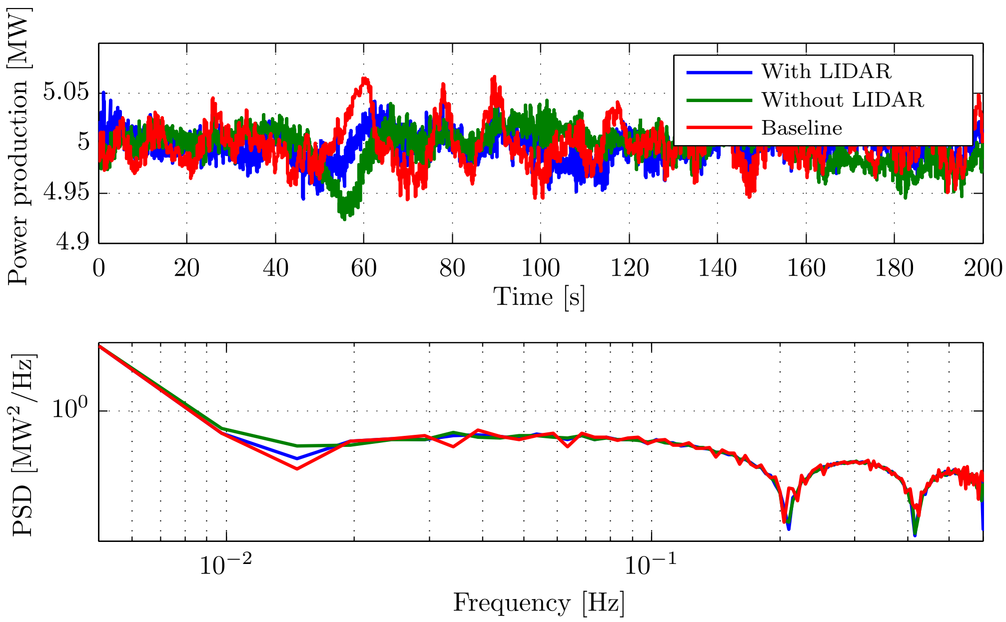

Figure 6.2: Power production and the corresponding PSD.

A constant rotor speed (12.1 rpm) is wanted when operating in region 3. Figure 6.3 on the next page shows the rotor speed for the three controllers. All of the controllers perform similar. Fluctuations at 60 seconds are observed as expected from the gust shown in figure 6.1 on the preceding page.

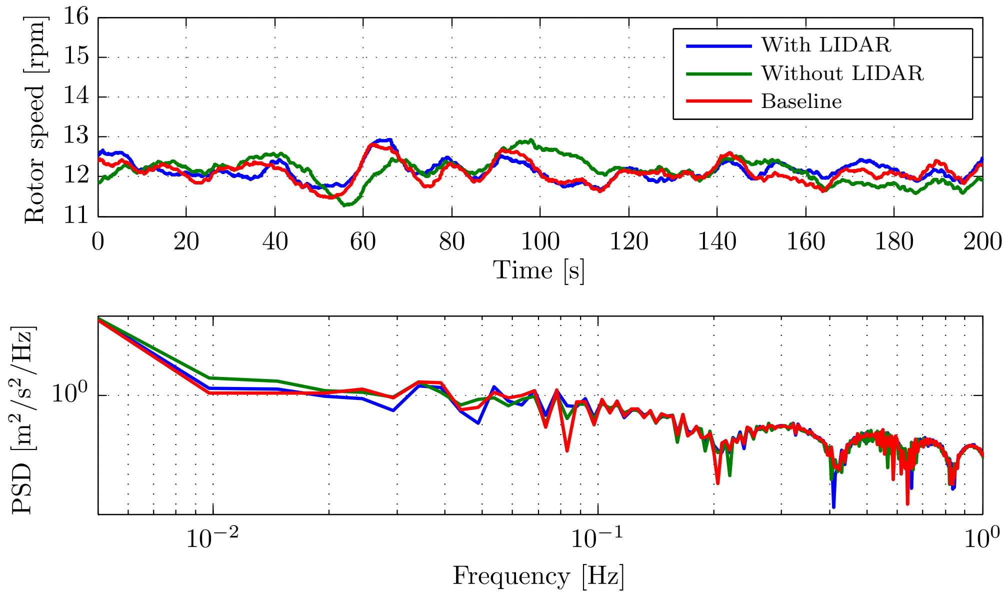

Figure 6.3: Rotor speed and the corresponding PSD.

As little fore-aft tower oscillation as possible is wanted to reduce the stresses in the tower structure. The fore-aft tower deflection is shown in figure 6.4, where it is observed that once again that the controllers perform similarly. The same applies for the low-speed shaft torsion as shown in figure 6.5 on the following page, where no clear winner emerges.

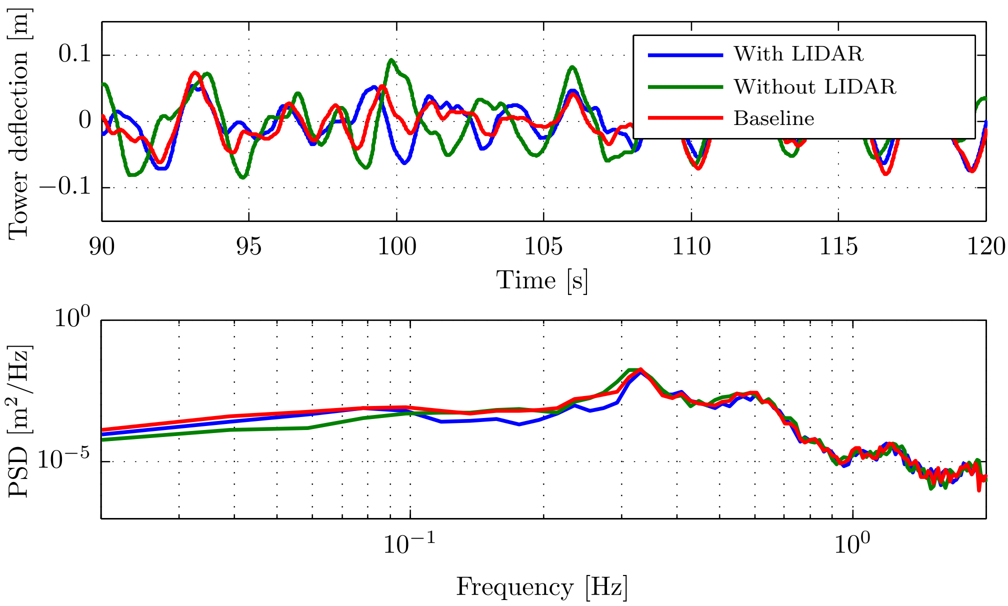

Figure 6.4: Fore-aft tower deflection and the corresponding PSD.

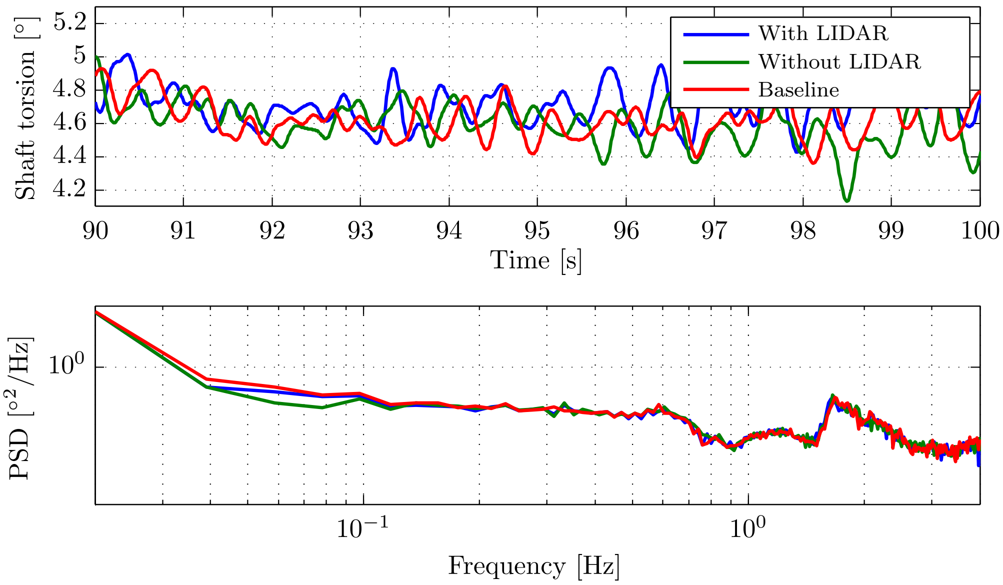

Figure 6.5: Low-speed shaft torsion and the corresponding PSD.

So far no evidence for performance improvement with LIDAR has been shown. This is however not the case for the flapwise blade bending moments of the blades as shown in figure 6.6 on the next page. The reduction of the flapwise blade bending moments are greatest at $1P$ (0.2 Hz). However, reductions at $2P$, $3P$, and $4P$ are also achieved. The edgewise blade bending moments show no improvements, as shown in figure 6.7 on the facing page. This is expected since the flapwise blade bending moments has a low weight in the cost function for low pitch angles because edgewise blade bending moments do not affect the axial bending moments at low pitch angles.

The $1P$ frequency reduction for the flapwise blade bending moments plays a key role in reducing the loads in the bearings caused by pitching of the nacelle and the tip moments of the low-speed shaft. Only the loads at the tip of the low-speed shaft is shown since the loads in the bearing shows similar reductions, since they represent the same loads. The reductions for the tip moments of the low-speed shaft are shown in figure 6.8 on page 60 for a non rotating reference frame and in figure 6.9 on page 60 for a rotor fixed reference frame, i.e. a rotating reference frame. Both figures show reductions in the loads, which is evident in both the time series and the PSD. The reductions for the loads in the non rotating reference frame are located at $1P$ and at $3P$, which makes sense since the $1P$ frequency was reduced for the flapwise blade bending moments in the rotating reference frame. The reductions for the loads in the rotating reference frame are primarily located at $1P$, $2P$, $3P$, and $4P$.

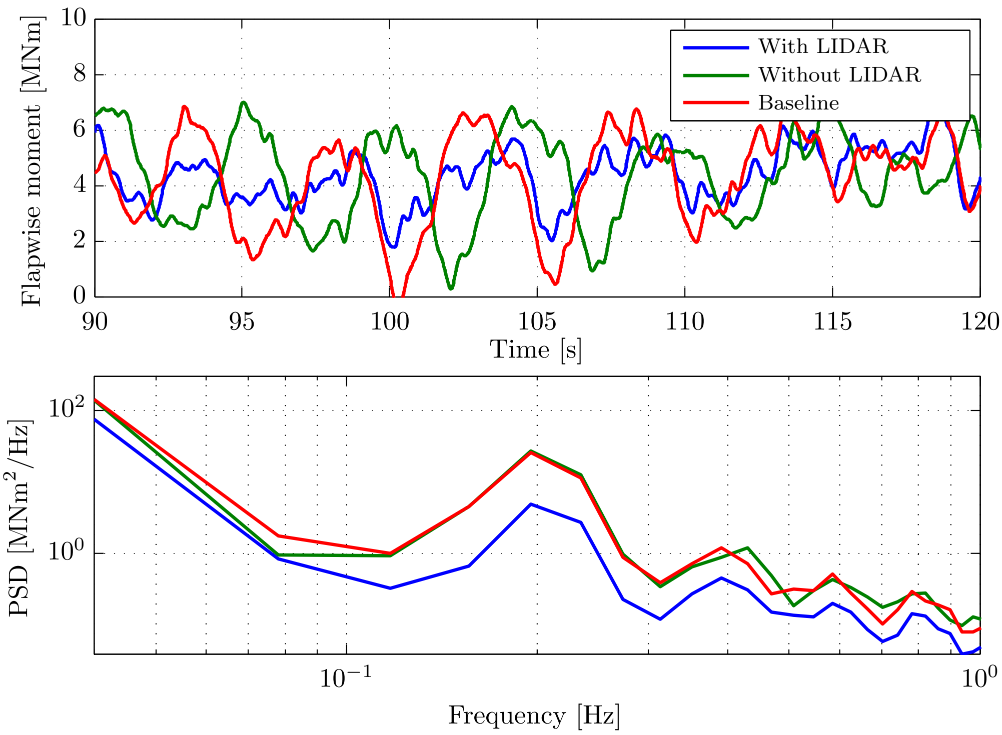

Figure 6.6: Flapwise blade bending moment and the corresponding PSD.

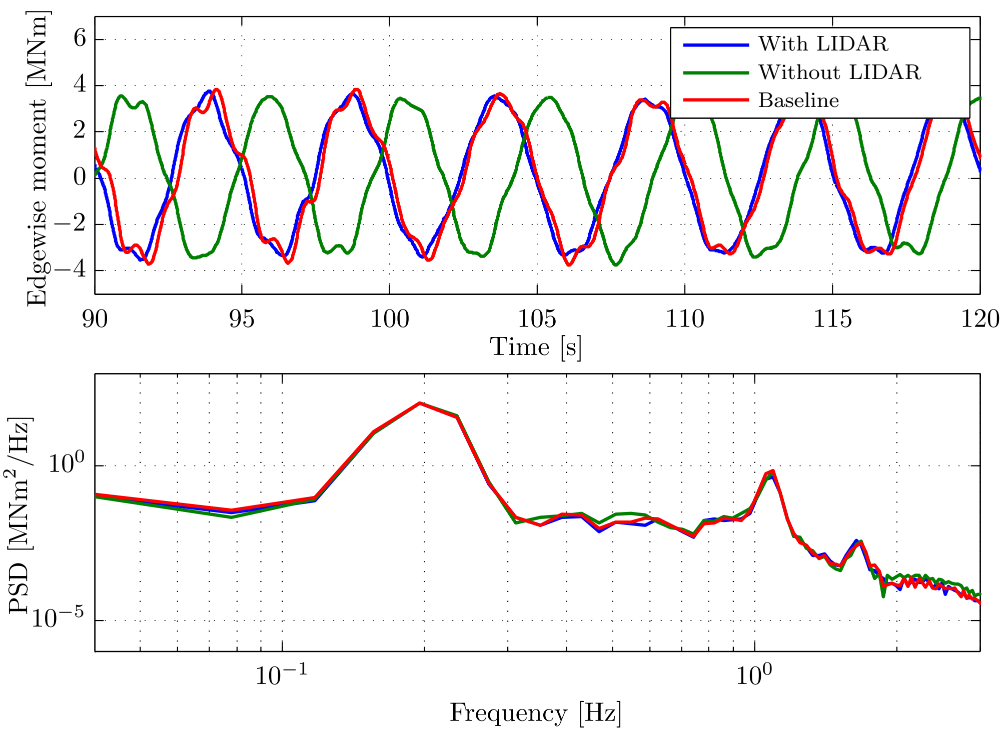

Figure 6.7: Edgewise blade bending moment and the corresponding PSD.

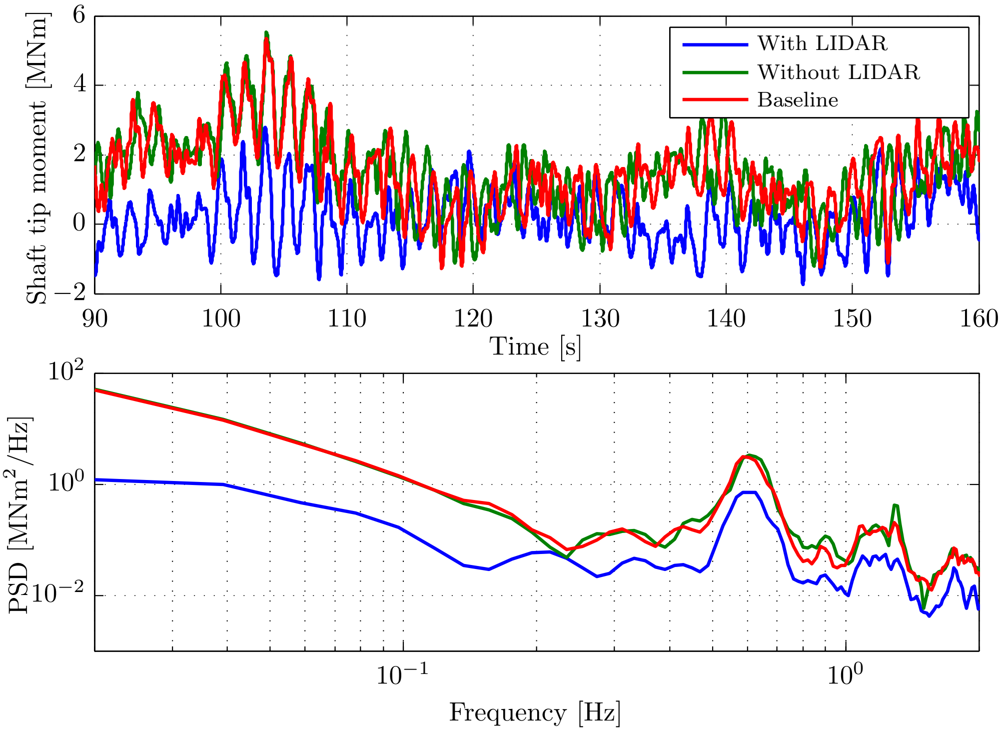

Figure 6.8: Tip moments of the low-speed shaft (nonrotating) and the PSD.

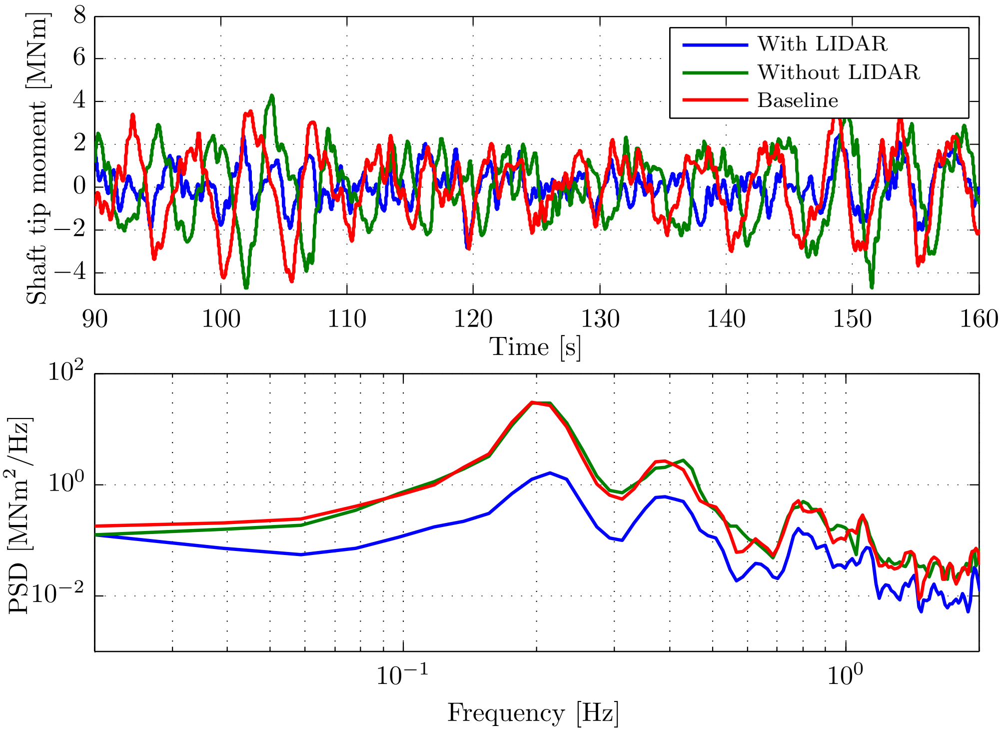

Figure 6.9: Tip moments of the low-speed shaft (rotating) and the PSD.

The reductions need to be compared to the activity of the actuators. The generator torque is shown in figure 6.10, where the actuation of the controllers is similar. When looking at the pitch angle in figure 6.11 an increased activity is observed for the LIDAR based controller as expected. The cyclic pitch effect observed is due to the vertical wind shear, and this frequency is at $1P$ (0.2 Hz).

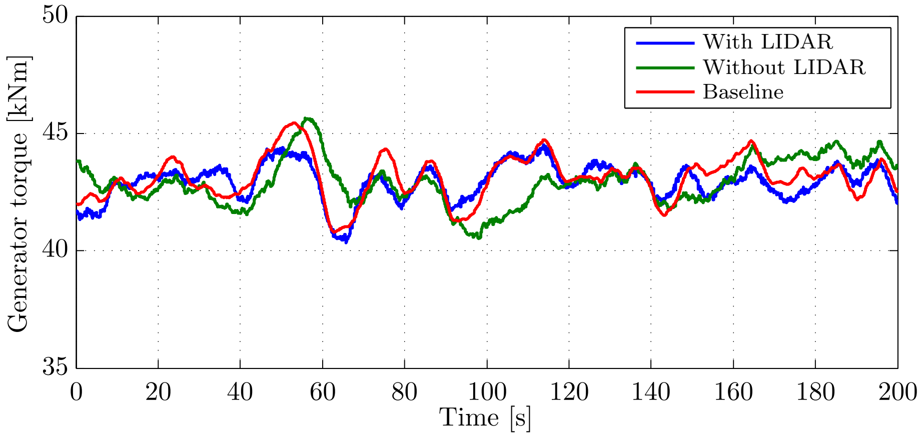

Figure 6.10: Applied generator torque.

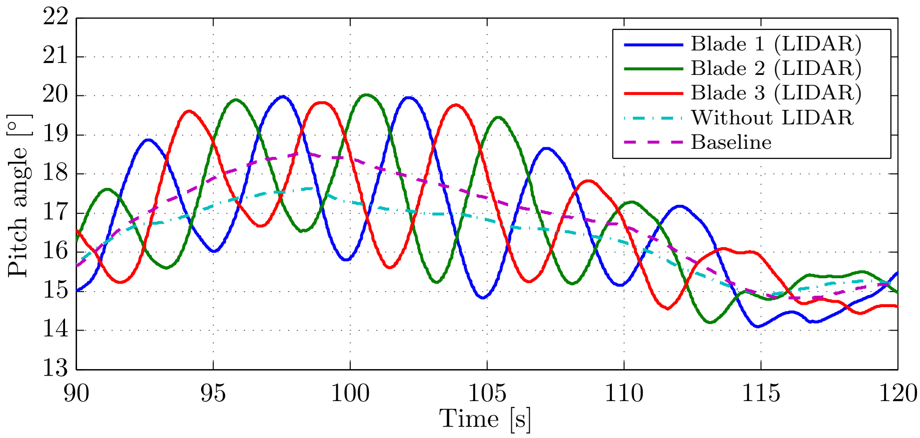

Figure 6.11: Pitch angle.

The results have shown that the MPC without LIDAR performs similar to the NREL Baseline controller and that it is the LIDAR that provides the difference in the results. A summary of the most important load reduction results is shown in table 6.1 on the next page, where the two MPCs are compared to the baseline controller. Furthermore the Damage Equivalent Loads (DEL) reductions are calculated as well according to (ASTM International, 2011) and are calculated using a rainflow counting toolbox for Matlab (Nieslony, 2010).

	Without LIDAR	With LIDAR
Flapwise bending moment at $1P$	0 %	-60 %
Edgewise bending moment at $1P$	0 %	0 %
Tip moment of the low-speed shaft (non-rotating) at $3P$	0 %	-66 %
Tip moment of the low-speed shaft (rotating) at $1P$	0 %	-85 %
Tower deflection DEL	9.5 %	-7.7 %
Low-speed shaft torsion DEL	-4 %	-6 %
Flapwise moments DEL	-6.6 %	-17.4 %
Edgewise moments DEL	-1.1 %	-1.8 %
Tip moment of the low-speed shaft (non-rotating) DEL	0.8 %	-32.5 %
Tip moment of the low-speed shaft (rotating) DEL	0.7 %	-33.6 %

Table 6.1: Comparison of loads of the wind turbine. Shown are the percentage reductions in the loads compared to the NREL Baseline controller. The $1P$ frequency load reduction are based on the PSDs. Negative numbers indicate reductions and positive numbers indicate increased loads compared to the NREL Baseline controller.

The power production sample variance is computed to assist the comparison of the power production quality of each of the controllers. The variances for each of the controllers are:

MPC with LIDAR: 203 10^{-6} MW^2

MPC without LIDAR: 326 10^{-6} MW^2

NREL Baseline: 428 10^{-6} MW^2

This shows that the LIDAR is able to significantly reduce the sample variance of the power production compared to the controllers without LIDAR, thus improving the power quality.

The results shown are tuned with a heavy weight on the asymmetric loads. By shifting the weights it would be possible to reduce other loads with lesser reductions in asymmetric loads.

Chapter 7

Conclusion

The purpose of this project was to show the possibilities of using LIDAR to reduce asymmetric loads while maintaining a given power level for a wind turbine. To utilize the preview wind information provided by the LIDAR an individual pitch strategy was used. The controller chosen to perform this strategy was MPC, which handles previews of disturbances in a natural way. Furthermore MPC is also able to handle the constraints of the actuators of the wind turbine.

MPC is a model based control scheme so a linear model was developed. The linear model was based on a BEM model and a linear dynamical model of the structure, pitch actuators, and drivetrain. The BEM model and the dynamical model together is a nonlinear model which was linearized at 18 m/s for the tests. Verification of the model showed it was well suited for control purposes.

Since the goal was to reduce asymmetric loads, a linear expression for these usable for MPC was wanted. That however was not possible without scheduling very frequently by the azimuth angle of the rotor. Instead the summed squared expression of those were introduced in the weights of the cost function of MPC via the Coleman transformation which yielded an expression with no dependence on the azimuth angle.

Along with the linear model, continuous wave LIDAR was chosen over pulsed LIDAR due to its ability to sample very fast and still have small errors at small preview distances. The preview distance of the LIDAR was chosen to be 54 m (corresponding to 3 seconds for a mean wind of 18 m/s) which gives the controller enough time to pitch the blades while still not introducing significant measurement errors.

Two MPCs were designed, one with LIDAR and one without LIDAR. These two controllers were then compared to the NREL Baseline controller. The baseline controller and the MPC without LIDAR performed similar. Results showed that the LIDAR based controller was able to reduce the asymmetric loads significantly while maintaining the power at 5 MW. Furthermore damage equiavalent loads were computed and compared for the three controller, which also showed that the LIDAR was able to reduce the damage equivalent loads. These reductions was however paid for with higher pitch acitity.

7.1 Further work

In order to use the LIDAR based MPC presented in this project on a real wind turbine a number of issues have to be addressed. The controller has not been designed with real-time operation in mind. Real-time operation could be done by using Fast MPC (Wang and Boyd, 2010) where the structure of the MPC problem is exploited. Other methods to enable MPC to run in real-rime is to use a precomputed lookup table or by making the horizons shorter.

The MPC with LIDAR is only designed for region 3 operation, so adjustments has to be made for the controller to work in region 1 and 2. Gain scheduling could be introduced to give the controller better performance and enable it to operate in the other regions although the controller would have to be modified slightly in region 1 and 2 to control for maximum power capture.

As stated in chapter 3 on page 13, LIDAR has a number if limitations and several assumptions are made in this project. These assumptions need to be dealt with in order to use LIDARs for real production turbines. Another improvement could be to introduce the effect of tower shadow in the model to make the predictions more accurate.

In this project all state measurements are taken directly from FAST, even those that are not normally measurable. To overcome this issue a state observer could be introduced to estimate the unmeasured states. Lastly, stability must be guaranteed for MPC in order to use it for a real wind turbine.

Bibliography

Aeolus (2008), *Photo of offshore wind farm at Horns Rev.*
URL: `http://www.ict-aeolus.eu/about.html`

ASTM International (2011), 'Standard practices for cycle counting in fatigue analysis', *ASTM E1049-85* .

Bianchi, F. D., De Battista, H. and Mantz, R. J. (2007), *Wind Turbine Control Systems*, Springer.

Bir, G. (2008), 'Multiblade coordinate transformation and its application to wind turbine analysis', *ASME Wind Energy Symposium* .

Bossanyi, E. A. (2003*a*), 'Individual blade pitch control for load reduction', *Wind Energy,* **6**, pp. 119–128.

Bossanyi, E. A. (2003*b*), 'Wind turbine control for load reduction', *Wind Energy,* **6**, pp. 229–244.

Bossanyi, E. A. (2005), 'Further load reductions with individual pitch control', *Wind Energy,* **8**, pp. 481–485.

Braña, I. (2001), *Turbine-Mounted Lidar:The pulsed lidar as a reliable alternative*, Gotland University.

BTM Consult (2010), 'World market update 2010. forecast 2011-2015', *International Wind Energy Development* .

Buhl, M. (2011), *WT-Perf*, National Renewable Energy Laboratory.
URL: `http://wind.nrel.gov/designcodes/simulators/wtperf/`

Dunne, F., Simley, E. and Pao, L. Y. (2011), 'Lidar wind speed measurement analysis and feed-forward blade pitch control for load mitigation in wind turbines'.

Hansen, M. O. L. (2008), *Aerodynamics of Wind Turbines*, Earthscan.

Jelavić, M., Petrović, V. and Perić, N. (2010), 'Estimation based individual pitch control of wind turbine', *Automatika,* **51**, pp. 181–192.

Johnson, K., Pao, L., Balas, M. and Fingersh, L. (2006), 'Standard and adaptive techniques for maximizing energy capture', *IEEE Control Systems Magazine,* **26**(3), pp. 70–81.

Jonkman, B. J. (2009), *TurbSim User's Guide*, National Renewable Energy Laboratory.
URL: `http://wind.nrel.gov/designcodes/preprocessors/turbsim/TurbSim.pdf`

Jonkman, J. M., Butterfield, S., Musial, W. and Scott, G. (2009), *Definition of a 5-MW Reference Wind Turbine for Offshore System Development*, National Renewable Energy Laboratory.

Jonkman, J. M. and Jr., M. L. B. (2005), *FAST User's Guide*, National Renewable Energy Laboratory.
URL: `http://wind.nrel.gov/designcodes/simulators/fast/FAST.pdf`

Kanev, S. and van Engelen, T. (2010), 'Wind turbine extreme gust control', *Wind Energy,* **13**, pp. 18–35.

Laks, J., Pao, L., Wright, A., Kelley, N. and B.Jonkman (2010), 'Blade pitch control with preview measurements', *Proc. AIAA Aerospace Sciences Meeting,* .

Laks, J., Pao, L. Y., Simley, E., Wright, A. D., Kelley, N. and Jonkman, B. (2011), 'Model predictive control using preview measurements from lidar', *Proc. AIAA Aerospace Sciences Meeting* .

Maciejowski, J. M. (2000), *Predictive Control with Constraints*, Prentice Hall.

Nieslony, J. (2010), *Rainflow Counting Algorithm.*
URL: `http://www.mathworks.com/matlabcentral/fileexchange/3026-rainflow-counting-algorithm`

Simley, E., Pao, L. Y., Frehlich, R., Jonkman, B. and Kelley, N. (2011), 'Analysis of wind speed measurements usingcontinuous wave lidar for wind turbine control', *Proc. AIAA Aerospace Sciences Meeting* .

Soltani, M., Wisniewski, R., Brath, P. and Boyd, S. (2011), 'Load reduction of wind turbines using receding horizon control', *IEEE International Conference on Control Applications* .

Vestas (2012), *Photo of Vestas V112-3.0 MW wind turbine*.
URL: `http://www.vestas.com/en/media/images.aspx#Vindmoeller`

Wang, Y. and Boyd, S. (2010), 'Fast model predictive control using online optimization', *IEEE Transactions on Control Systems Technology* .

Appendix A

Nomenclature

Acronyms and abbreviations are listed in alphabetical order. Symbols are listed after appearance in the thesis.

Acronyms and abbreviations

BEM Blade Element Momentum.

CW Continuous Wave.

DEL Damage Equivalent Load.

DFIG Double Fed Induction Generator.

DOF Degrees Of Freedom.

FAST Fatigue, Aerodynamics, Structures, and Turbulence.

HAWT Horizontal Axis Wind Turbine.

LIDAR Light Detection And Ranging.

LOS Line Of Sight.

MPC Model Predictive Control.

NREL National Renewable Energy Laboratory.

PSD Power Spectral Density.

VAWT Vertical Axis Wind Turbine.

Symbols

LIDAR

θ_{el} Elevation angle of LIDAR beam.

r Scan radius.

R Rotor radius.

D Preview distance.

T_p Preview time.

Model

d Disturbance vector.

V_i Wind input to the i'th blade.

β Blade pitch vector.

β_i Blade pitch for the i'th blade.

M_b Axial blade moment vector.

$M_{b,i}$ Axial blade moment for the i'th blade.

F_T Thrust force on the tower.

$\dot{x}_t$ Fore-aft tower velocity.

β_{ref} Blade pitch reference vector.

$\dot{\beta}$ Blade pitch rate vector.

T_r Rotational torque of the rotor.

T_g Generator torque.

ω_r Rotational speed of the rotor.

ω_g Rotational speed of the generator.

θ Low-speed shaft torsion.

$\dot{\theta}$ Low-speed shaft torsion speed.

P_e Produced electrical power.

Aerodynamics

V_0 Free stream wind speed.

A_0 Airflow area in front of the wind turbine.

V_D Wind speed at the rotor disc.

A_D Area of the rotor disc.

$V_{-\infty}$ Wind speed far behind the wind turbine.

$A_{-\infty}$ Airflow area far behind the wind turbine.

p_0 Atmospheric pressure.

p_D^+ Pressure immediatly in front of the rotor disc.

p_D^- Pressure immediatly behind the rotor disc.

ρ Density of the air.

F_D Force developed by the rotor disc.

a Axial induction factor.

P_D Power captured by the rotor disc.

C_P Power coefficient.

λ Tip speed ratio.

β_c Collective blade pitch.

V_{rot} Rotation speed of the wind at the rotor.

a' Tangential induction factor.

r_l Local radius of the rotor disc.

N_B Number of annular elements.

r_j Distance from the center of the hub.

Δr_j Width of element.

V_w Incoming relative free stream wind speed.

ϕ_j Local inflow angle.

$V_{\text{eff,j}}$ Local effective wind speed.

α_j Local angle of attack.

$\beta_{\text{tw,j}}$ Local twist of blade element.

$C_{\text{l,j}}$ Local lift coefficient.

$C_{\text{d,j}}$ Local drag coefficient.

L_j Local lift force.

D_j Local drag force.

c_j Chord length.

$T_{\text{r,i}}$ Rotational torque.

$F_{\text{T,i}}$ Thrust force.

$M_{\text{b,i}}$ Blade bending moment

F_P Prandtl's correction factor.

σ_j Solidity factor.

C_n Axial force coefficients.

C_t Tangential force coefficients.

F_{tip} Prandtl's tip loss factor.

F_{root} Prandtl's root loss factor.

B Number of blades.

Structure

ψ_i Azimuth angle of blade i

q_0 Collective term.

q_c Cosine-cyclic term.

q_s Sine-cyclic term.

M_{tilt} Tilt moment.

M_{yaw} Yaw moment.

T_c Coleman transformation matrix.

x_t Fore-aft tower deflection.

M_t Equivalent mass of the tower.

K_t Tower stiffness.

B_t Tower damping.

Pitch Actuators

τ_β Pitch time constant.

$\beta_{\text{ref,i}}$ Pitch reference for the i'th blade.

$\beta_{\min}$ Minimum pitch angle.

$\beta_{\max}$ Maximum pitch angle.

β_{rate} Maximum pitch rate.

Drivetrain

J_r Rotor inertia.

J_g Generator inertia.

K_θ Rotational stiffness.

B_θ Rotational damping.

N Gear ratio.

Generator

η_g Generator energy conversion efficiency.

T_{gmin} Minimum generator torque.

T_{gmax} Maximum generator torque.

T_{grate} Maximum change in generator torque.

Linearization

x_n State vector.

u_n Input vector.

d_n Disturbance vector.

z_n Output vector.

f System equations.

h Output equations.

x Linearized states.

u Linearized inputs.

d Linearized disturbances.

z Linearized outputs.

A System matrix.

B_u Input matrix.

B_d Disturbance input matrix.

C Output matrix.

D_u Input direct term.

D_d Disturbance direct term.

Controller

J_z Cost function of the outputs.

$J_{\Delta u}$ Cost function of the control moves.

J Combined cost function.

H_p Prediction horizon.

H_u Control horizon.

Q Output weighting matrix.

R Input weighting mattix.

$\mathcal{Z}$ Predicted outputs over the prediction horizon.

$\Delta\mathcal{U}$ Predicted control moves over the control horizon.

$\mathcal{D}$ Disturbances over the prediction horizon.

Ψ Initial state to output matrix.

Υ Previous input to output matrix.

Θ Predicted control moves to outputs matrix.

Ξ Disturbances to output matrix.

E Control moves contraint matrix.

G Input constraint matrix.

L Output constraint matrix.

g Last column of G.

Γ The first H_u columns of L.

l Last column of L.

Λ The first H_u columns of E.

e Last column of E.

$\mathcal{T}$ Is the Coleman matrix multiplied by its transpose.

Q_w Diagonal matrix containing output weights.

Appendix B

Parameters for the Model

Parameters for the model are summarised in table B.1 on the next page. The aerodynamic data for the blades, that is blade elements and lift and drag coefficient curves, are collected from the FAST files for the 5 MW reference turbine.

Parameter	Description	Value	Unit
Aerodynamics			
ρ	Air density	1.225	$kg \cdot m^{-3}$
R	Rotor radius	63	m
Pitch Actuator			
τ_β	Pitch time constant	0.05	s
β_{min}	Lower pitch limit	0	deg
β_{max}	Upper pitch limit	90	deg
$\dot{\beta}_{max}$	Maximum pitch rate	8	$deg \cdot s^{-1}$
Drivetrain			
J_r	Moment of inertia of rotor and hub	35.444×10^6	$kg \cdot m^2$
J_g	Moment of inertia of generator	534.116	$kg \cdot m^2$
B_θ	Shaft torsion damping coefficient	3.453×10^6	$N \cdot s \cdot m^{-1}$
K_θ	Shaft torsion spring coefficient	510.370×10^6	$N \cdot m^{-1}$
N	Gear ratio	97	-
Structure			
M_t	Equivalent mass	472.5×10^3	kg
B_t	Equivalent damping coefficient	19.2×10^3	$N \cdot s \cdot m^{-1}$
K_t	Equivalent spring coefficient	1.96×10^6	$N \cdot m^{-1}$
Generator			
η_g	Generator efficiency	0.944	-
T_{gmin}	Minimum generator torque	0	$N \cdot m$
T_{gmax}	Maximum generator torque	43,093.55	$N \cdot m$
T_{grate}	Maximum rate of change of the generator torque	15,000	$N \cdot m \cdot s^{-1}$

Table B.1: Model parameters.

Appendix C

Power Coefficient Surface

Graph of the power coefficient surface is shown in figure C.1. The power coefficients are found using the tool WT-perf (Buhl, 2011). WT-perf is a tool used to predict performance of a wind turbine and uses Blade Element Momentum theory to do so.

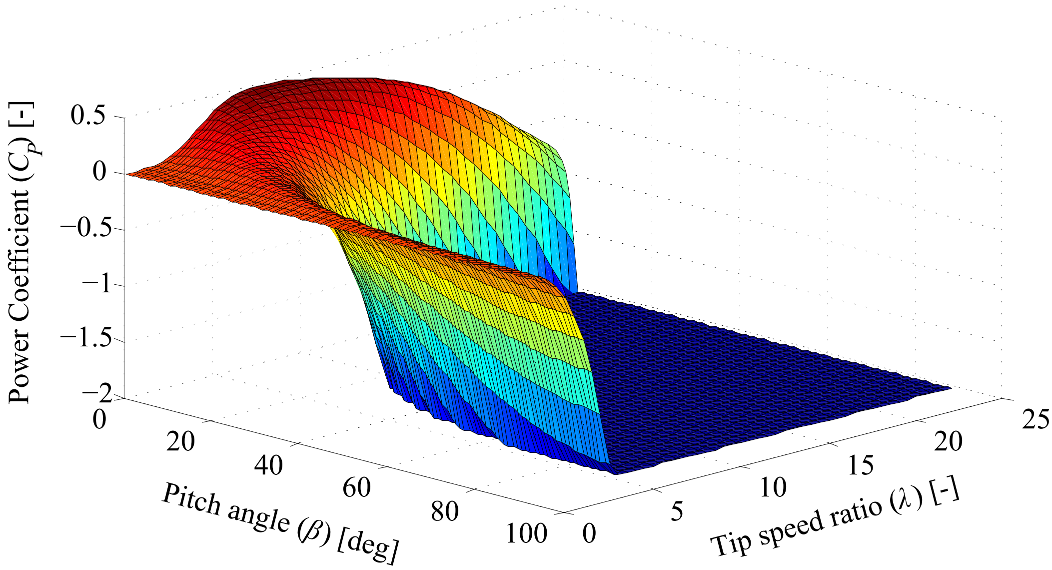

Figure C.1: Power coefficient surface.